https://doi.org/10.5194/wes-2022-62
Preprint. Discussion started: 7 July 2022

eawe european academy of wind energy
Open Access WIND ENERGY SCIENCE DISCUSSIONS

Evaluation of lidar-assisted wind turbine control under various turbulence characteristics

Feng Guo[1], David Schlipf[1], and Po Wen Cheng[2]

[1]Wind Energy Technology Institute, Flensburg University of Applied Sciences, Kanzleistraße 91-93, 24943 Flensburg, Germany
[2]Stuttgart Wind Energy (SWE), Institute of Aircraft Design, University of Stuttgart, Allmandring 5b, 70569 Stuttgart, Germany

Correspondence: Feng Guo (feng.guo@hs-flensburg.de)

Abstract. Lidar systems installed on the nacelle of wind turbines have the capability to provide a preview of incoming turbulent wind. Lidar-assisted wind turbine control (LAC) allows the turbine controller to react to changes in the wind before they affect the wind turbine. Currently, the most proven LAC technique is the collective pitch feed-forward control, which has been found to be beneficial for load reduction. In literature, the benefits were mainly investigated using standard turbulence parameters suggested by the IEC 61400-1 standard and assuming Taylor's frozen hypothesis (the turbulence measured by the lidar propagates unchanged to the rotor). In reality, the turbulence spectrum and the spatial coherence change by the atmospheric stability conditions. Also, Taylor's frozen hypothesis does not take into account the coherence decay of turbulence in the longitudinal direction. In this work, we consider three atmospheric stability classes: unstable, neutral, and stable, and generate four-dimensional stochastic turbulence fields based on two models: the Mann model and the Kaimal model. The generated four-dimensional stochastic turbulence fields include the longitudinal coherence thus avoiding assuming Taylor's frozen hypothesis. The Reference Open Source Controller (ROSCO) is used as the baseline feedback-only controller. A reference lidar-assisted controller (LACer) is developed and used to evaluate the benefit of LAC. Considering the NREL 5.0 MW reference wind turbine and a typical four-beam pulsed lidar system, it is found that the filter design of the LACer is not sensitive to the turbulence characteristics representative of the investigated atmospheric stability classes. The benefits of LAC are analyzed using the aeroelastic tool OpenFAST. According to the simulations, LAC's benefits are mainly the reductions in rotor speed variation (15% to 40%), tower fore-aft bending moment (2% to 18.8%), and power variation (3% to 20%). This work reveals that the benefits of LAC can depend on the turbulence models, the turbulence characteristics, and the mean wind speed.

1 Introduction

Traditionally, wind turbine control only relies on the feedback(FB) control strategy. For above-rated wind operations, the rotor speed change caused by the turbulence wind is measured and the pitch is activated to maintain the rated rotor speed. This means that the turbine reacts to wind disturbances only after they have been affected. A nacelle lidar scanning in front of the turbine can provide a preview of the incoming turbulence. Based on the preview, a rotor effective wind speed (REWS) can be derived and used to provide a forward pitch signal. The forward pitch signal can be simply added to the conventional feedback

https://doi.org/10.5194/wes-2022-62
Preprint. Discussion started: 7 July 2022

eawe european academy of wind energy
Open Access WIND ENERGY SCIENCE DISCUSSIONS

control (Schlipf, 2015), which is often referred to as Lidar-assisted collective pitch feedforward control(CPFF). Apart from CPFF, there are other LAC concept has have been presented in literature (Schlipf et al., 2013b; Schlipf, 2015; Schlipf et al., 2020). While CPFF is so far the most promising technology and it has been deployed in commercial projects (Schlipf et al., 2018b). Thus we focus on assessing the benefits of CPFF in this work.

In order to utilize the lidar measurement for LAC, a correlation study is necessary to determine how much the lidar estimated REWS is correlated with the actual REWS acting on the turbine rotor. Some facts that could have an impact on the measurement correlation are listed below:

(a) Lidar measurement positions. Lidar has fewer measurement points within the rotor-swept area compared to the rotational sampling rotor. Thus, the lidar estimated REWS is less spatially filtered;

(b) Line-of-sight (LOS) wind speed v_{los} measurement, which is the cumulative projection of longitudinal (u), lateral (v) and vertical (w) components in the lidar beam direction. The lidar measurements can be contaminated by lateral and vertical wind speed components (Held and Mann, 2019), because of the beam opening angles, the nacelle movement, or the turbine yaw misalignment;

(c) Lidar probe volume. The measurement by lidar is the weighted averaging of LOS along the lidar beam (Peña et al., 2013; Peña et al., 2017);

(d) Turbulence spectrum and coherence. The lidar measurement coherence is mathematically derived based on the spectrum and coherence (Schlipf, 2015; Held and Mann, 2019; Guo et al., 2022a).

(e) Atmospheric stability. The turbulence spectrum and coherence have been shown to vary by atmospheric stability conditions (Peña, 2019; Guo et al., 2022a).

According to the IEC standard, two turbulence models are commonly used for wind turbine design as provided by the IEC 61400-1:2019 standard, they are the Mann uniform shear model Mann (1994) and the Kaimal spectra Kaimal et al. (1972) and exponential coherence model (hereafter referred as to Mann model and Kaimal model respectively). The derivation of lidar measurement coherence based on a specific turbulence model has been studied in the literature. For example, Schlipf et al. (2013a); Schlipf (2015) shows the derivation by Kaimal spectra and exponential coherence model. Mirzaei and Mann (2016); Held and Mann (2019); Guo et al. (2022a) demonstrate the solution for Mann model.

Once the lidar measurement coherence is analyzed, a filter needs to be designed to filter out uncorrelated information in the lidar estimated REWS. Since the filter introduces a certain time delay (Schlipf, 2015), a timing algorithm is necessary to ensure the turbine feed-forward pitch act at the correct time. Usually, the time that turbulence requires to propagate from upstream to downstream, the time delay in the pitch actuator, and the time delay caused by filtering should all be considered. In this work, we will contribute by providing a reference lidar-assisted controller. It includes 1) a lidar data processing module that estimates the lidar-based REWS, 2) a feed-forward rate provider and 3) a modified ROSCO feed-back controller.

When evaluating the benefits of LAC, (Schlipf, 2015) uses the Kaimal model with the turbulence spectral parameters provided by the IEC standard Schlipf (2015) through FAST(the previous version of OpenFAST) aeroelastic simulation. With a

https://doi.org/10.5194/wes-2022-62
Preprint. Discussion started: 7 July 2022

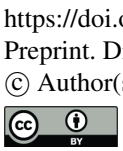

eawe european academy of wind energy
Open Access WIND ENERGY SCIENCE DISCUSSIONS

circular scanning lidar, LAC is found to bring a noticeable reduction in the lifetime damage equivalent load (DEL) in the tower base fore-aft bending moment, the low-speed shaft torque, and the blade root out-of-plane moment. However, the variations of turbulence parameters have not been considered.

The recent developments in the turbulence simulation tool: *evoturb* by Chen et al. (2022) and *4D-Mann-Turbulence-Generator* by Guo et al. (2022a) have made it possible to integrate turbulence evolution into aeroelastic simulation. With the updated OpenFAST lidar simulator Guo et al. (2022b), the 4D turbulence field can be imported into OpenFAST, and the upstream lidar measurement can be simulated using the upstream turbulence fields.

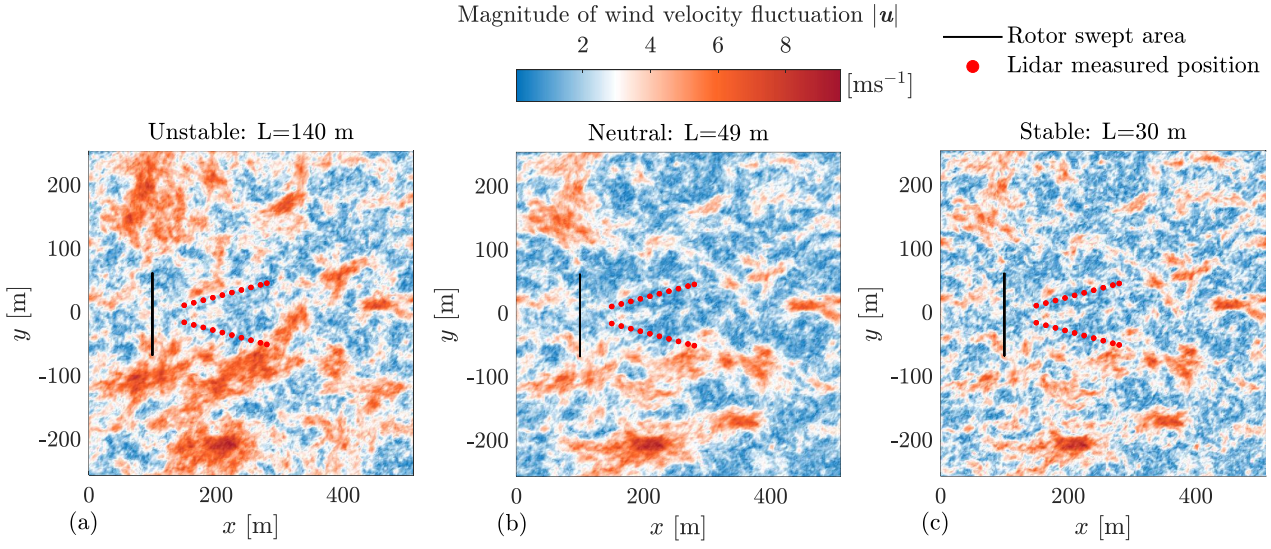

Figure 1. Top view of a turbulence field showing the eddy structures under different atmospheric stability. Simulated using the 4D Mann turbulence generator with parameters listed in Table 1. The lidar measured positions are plotted based on a typical four-beam pulse lidar. And the rotor swept-area is drawn based on the NREL 5.0MW reference wind turbine which has a rotor diameter of 126 m.

The variation of turbulence parameters from the standard value given by IEC 61400-1:2019 can be interesting for wind energy. Turbulence parameters under different atmospheric stability are investigated and summarized by e.g. Cheynet et al. (2017); Peña (2019); Nybø et al. (2020). For example, Figure 1 shows how the turbulence structure changes by the length scale L. A larger coherent eddy structure is observed in the unstable stability and the eddy structure is much smaller in size under the stable stability. In the neutral case, the eddy structure is somewhere between the two cases. The length scale can have an impact on the power spectrum and turbulence spatial coherence. Further, the spectrum and coherence can have potential impacts not only on the lidar measurement coherence but also on the turbine loads. Because the turbulence spectrum peaks can distribute at different frequency ranges and different frequencies can produce different excitations for the turbine structure motion.

In this work, we summarize how the turbulence spectrum and spatial coherence can vary by atmospheric stability from literature. Three atmospheric stability classes: unstable, neutral, and stable are considered. For each atmospheric stability class, the Mann model parameters are collected, and then the Kaimal model parameters are fitted to have similar spectra

https://doi.org/10.5194/wes-2022-62
Preprint. Discussion started: 7 July 2022

eawe european academy of wind energy
Open Access WIND ENERGY SCIENCE DISCUSSIONS

and coherence as compared to the Mann model. Then the four-dimensional stochastic turbulence fields are generated using *4D-Mann-Turbulence-Generator* (Guo et al., 2022a) and *evoturb* (Chen et al., 2022). The benefits of LAC are then assessed using a typical four-beam commercial lidar configuration and the 5MW reference wind turbine by NREL (Jonkman et al., 2009) through the lidar simulator-integrated aeroelastic simulation tool: OpenFAST. To compare CPFF with the traditional feedback-only controller, ROSCO is considered as the baseline feedback controller.

This paper is organized as follows: Section 2 gives the background about turbulence modelling; Section 3 discusses the correlation between the lidar estimated REWS and the turbine based REWS; Section 4 introduces the designing of lidar-assisted controller; Section 5 present and discuss the simulation results; Section 6 draws conclusions for this research.

2 Turbulence modeling

In this section, we first introduce Mann (1994) model and Kaimal et al. (1972) spectrum and exponential coherence model Davenport (1961) used in this work. Then, the methods to include turbulence evolution into the two turbulence models are discussed. Lastly, we calculate the turbulence spectra and coherence under different atmospheric stability classes.

2.1 Mann turbulence model

Mann (1994) model is a spectral tensor model recommended by the IEC 61400-1:2019 standard for wind turbine load calculations. It applies the rapid distortion theory (Hunt and Carruthers, 1990) to an isotropic spectral tensor based on the von Kármán (1948) energy spectrum, to model the shear stretched eddy structure.

At a certain moment, the velocity field can be described by $\tilde{\boldsymbol{u}}(\boldsymbol{x})$, with $\boldsymbol{x} = (x, y, z)$ the position vector in space (Cartesian coordinate). After applying Taylor's frozen hypothesis Taylor (1938) and Reynolds decomposition, the fluctuation part of the turbulence $\boldsymbol{u}(\boldsymbol{x}) = \tilde{\boldsymbol{u}} - \boldsymbol{U}$ about the mean flow $\boldsymbol{U} = (U, 0, 0)$ is assumed homogeneous in space and it can be computed from the Fourier transform

$$\boldsymbol{u}(\boldsymbol{x}, t_0) = \int \hat{\boldsymbol{u}}(\boldsymbol{k}, t_0) \exp(\mathrm{i}\boldsymbol{k} \cdot \boldsymbol{x}) \mathrm{d}\boldsymbol{k}, \tag{1}$$

where $\hat{\boldsymbol{u}}(\boldsymbol{k}, t_0)$ is the Fourier coefficient of the velocity field, i is the imaginary unit and $\int \mathrm{d}\boldsymbol{k} \equiv \int_{-\infty}^{\infty}\int_{-\infty}^{\infty}\int_{-\infty}^{\infty} \mathrm{d}k_1\mathrm{d}k_2\mathrm{d}k_3$ means the integration over all the wavenumber vectors $\boldsymbol{k} = (k_1, k_2, k_3)$. Conversely,

$$\hat{\boldsymbol{u}}(\boldsymbol{k}, t_0) = \frac{1}{(2\pi)^3} \int \boldsymbol{u}(\boldsymbol{x}, t_0) \exp(-\mathrm{i}\boldsymbol{k} \cdot \boldsymbol{x}) \mathrm{d}\boldsymbol{x}, \tag{2}$$

with $\int \mathrm{d}\boldsymbol{x} \equiv \int_{-\infty}^{\infty}\int_{-\infty}^{\infty}\int_{-\infty}^{\infty} \mathrm{d}x\mathrm{d}y\mathrm{d}z$. The Fourier coefficient is connected to the spectral tensor by

$$\Phi_{ij}(\boldsymbol{k})\delta(\boldsymbol{k} - \boldsymbol{k'}) = \langle \hat{u}_i{}^*(\boldsymbol{k}, t_0)\hat{u}_j(\boldsymbol{k'}, t_0)\rangle, \tag{3}$$

where $\langle\ \rangle$ means the ensemble average, * denotes the complex conjugate and $\delta()$ is the Dirac delta function. $\boldsymbol{k'}$ is also the wavenumber vectors and it is used to differentiate with $\boldsymbol{k}$. Equation (3) implies that the ensemble averages of the Fourier

https://doi.org/10.5194/wes-2022-62
Preprint. Discussion started: 7 July 2022

eawe european academy of wind energy
Open Access WIND ENERGY SCIENCE DISCUSSIONS

coefficients of non-identical wavenumber vectors are all zero. $i, j = 1, 2, 3$ are indexes that stand for u, v, and w components i.e. $\boldsymbol{u} = (u_1, u_2, u_3) = (u, v, w)$. The detailed expression of the spectral tensor $\boldsymbol{\Phi}$ can be found from Mann (1994). Except for the wavenumber vector, there are three other parameters in the model, they are:

— $\alpha\varepsilon^{2/3}$ [$\mathrm{m}^{4/3}\mathrm{s}^{-2}$]: a energy level constant valid in the inertial subrange, composed by the spectral Kolmogorov constant α and the rate of viscous dissipation of specific turbulent kinetic energy ε (Mann, 1998); This constant is actually acting as a proportional gain to the spectral tensor and it is often adjusted to obtain a specific turbulence intensity (TI).

— L [m]: a length scale related to the size of the eddies containing the most energy (Held and Mann, 2019);

— Γ [-]: a non-dimensional anisotropy due to shear effect in near-surface boundary layer. When $\Gamma = 0$, the turbulence is isotropic (Mann, 1994, 1998).

Mann (1994) uses Γ to calculate the eddy lifetime by

$$\tau(\boldsymbol{k}) = \Gamma\left(\frac{\mathrm{d}U}{\mathrm{d}z}\right)^{-1}(|\boldsymbol{k}|L)^{-\frac{2}{3}}\left[{}_2F_1\left(\frac{1}{3}, \frac{17}{6}; \frac{3}{4}; -(|\boldsymbol{k}|L)^{-2}\right)\right]^{-\frac{1}{2}}, \tag{4}$$

where ${}_2F_1()$ is a hypergeometric function and $\frac{\mathrm{d}U}{\mathrm{d}z}$ is the mean vertical shear profile. The eddy life time τ actually distort the wavenumber k_3 (corresponds to the z direction) from the initial shearless state k_{30} by $k_3 = k_{30} - \beta k_1$. Here, $\beta = \frac{\mathrm{d}U}{\mathrm{d}z}\tau$ is a non-dimensional distortion factor (Mann, 1994). The effect of the hypergeometric function ${}_2F_1()$ is to have

$$\tau(\boldsymbol{k}) \quad \begin{cases} \propto |\boldsymbol{k}|^{b_1}, & \text{for } |\boldsymbol{k}| \to \infty, \\ \propto |\boldsymbol{k}|^{b_2}, & \text{for } |\boldsymbol{k}| \to 0, \end{cases} \tag{5}$$

where b_1 and b_2 are two constants standing for the slopes of τ in logarithmic scale. Instead of using the hypergeometric function. Guo et al. (2022a) proposed another equation for the eddy lifetime

$$\tau(\boldsymbol{k}) = \Gamma\left(\frac{\mathrm{d}U}{\mathrm{d}z}\right)^{-1}\left[a\,(|\boldsymbol{k}|L)^{b_1}\left((|\boldsymbol{k}|L)^{10} + 1\right)^{\frac{b_2 - b_1}{10}}\right], \tag{6}$$

$$\text{with} \quad a = \left[{}_2F_1\left(\frac{1}{3}, \frac{17}{6}; \frac{3}{4}; -1\right)\right]^{-\frac{1}{2}}, \tag{7}$$

which is straight forward to adjust the slopes of the eddy-life time. And they found adjusting the slope constant b_1 for stable atmospheric stability tends to give better agreements of spectra and coherence between the model and the measurement from a lidar and a meteorological mast. We will use Equation (6) for the rest of this paper.

The one dimensional (along the longitudinal wavenumber) cross-spectra of all velocity components with separations Δy and Δz can be obtained by

$$F_{ij}(k_1, \Delta y, \Delta z) = \int \boldsymbol{\Phi}_{ij}(\boldsymbol{k}) \exp(\mathrm{i}(k_2\Delta y + k_3\Delta z))\mathrm{d}\boldsymbol{k}_\perp, \tag{8}$$

where $\int \mathrm{d}\boldsymbol{k}_\perp \equiv \int_{-\infty}^{\infty}\int_{-\infty}^{\infty}\mathrm{d}k_2\mathrm{d}k_3$. Specifically, when $i = j$ and $\Delta y = \Delta z = 0$, it becomes the auto-spectrum of one velocity component at one point, usually written as $F_{ii}(k_1)$. The magnitude squared coherence between two points in the same yz plane

https://doi.org/10.5194/wes-2022-62
Preprint. Discussion started: 7 July 2022

eawe european academy of wind energy
Open Access WIND ENERGY SCIENCE DISCUSSIONS

is often interested which can be calculated by (Mann, 1994)

$$\mathrm{coh}_{ij}^2(k_1,\Delta y,\Delta z)=\frac{|F_{ij}(k_1,\Delta y,\Delta z)|^2}{F_i(k_1)F_j(k_1)}. \tag{9}$$

2.2 Kaimal spectra and exponential coherence model

The Kaimal model given by IEC 61400-1:2019 uses the following formula to determine the auto-spectra of velocity components:

$$S_i(f)=\frac{4\sigma_i^2\frac{L_i}{U_{\mathrm{ref}}}}{(1+6f\frac{L_i}{U_{\mathrm{ref}}})^{5/3}} \tag{10}$$

where f is the frequency, L_i is the integral length scale, σ_i is the standard deviation, and U_{ref} is the reference wind speed equivalent to hub-height mean wind speed.

The coherence (with square) of the u components of two points in the yz plane is described as

$$\gamma_{yz}^2(\Delta yz,f)=\exp\left(-2a_{yz}r\sqrt{\left(\frac{f}{V_{\mathrm{hub}}}\right)^2+\left(\frac{0.12}{L_{\mathrm{c}}}\right)^2}\right), \tag{11}$$

with $\Delta yz=\sqrt{\Delta y^2+\Delta z^2}$ the separation distance, a_{yz} the coherence decay constant, and L_{c} the coherence scale parameter. Note that the coherence without square is used in IEC 61400-1:2019.

2.3 Modeling of turbulence evolution

The turbulence evolution refer as to the phenomenon that eddy structure changes when the turbulence propagates from upstream to down stream. And it is often represented using the longitudinal coherence.

2.3.1 Extending Mann model to include evolution

A space-time tensor which extends the three dimensional Mann spectral tensor $\mathbf{\Phi}$ to count for the temporal evolution of the turbulence field has been proposed by Guo et al. (2022a). The space-time tensor is evaluated to provide good agreements on the turbulence spectra and coherence including the spectra of all velocity components and the coherence of longitudinal, vertical-lateral, and all combined spatial separations. The validation has been made using data from a pulse lidar and a meteorological mast. Details of the model validation can be found in Guo et al. (2022a). The space-time tensor is written as:

$$\Theta_{ij}(\boldsymbol{k},\Delta t)=\exp\left(-\frac{\Delta t}{\tau_e(\boldsymbol{k})}\right)\Phi_{ij}(\boldsymbol{k}), \tag{12}$$

which defines the ensemble average

$$\Theta_{ij}(\boldsymbol{k},\Delta t)\delta(\boldsymbol{k}-\boldsymbol{k'})=\langle\hat{u}_i{}^*(\boldsymbol{k},t_0)\hat{u}_j(\boldsymbol{k'},t_0+\Delta t)\rangle, \tag{13}$$

where, $\hat{u}_j(\boldsymbol{k'},t_0+\Delta t)$ is the Fourier coefficient of the turbulence field at time $t_0+\Delta t$. τ_e is another eddy lifetime (different from τ) that defines the temporal evolution of the turbulence field and the expression

$$\tau_e(\boldsymbol{k})=\gamma\left[a\left(|\boldsymbol{k}|L\right)^{-1}\left(\left(|\boldsymbol{k}|L\right)^{10}+1\right)^{-\frac{2}{15}}\right], \tag{14}$$

https://doi.org/10.5194/wes-2022-62
Preprint. Discussion started: 7 July 2022

eawe european academy of wind energy
Open Access WIND ENERGY SCIENCE DISCUSSIONS

is found to predicts the longitudinal coherence well as investigated by Guo et al. (2022a). Here, γ is a parameter determines the strength of turbulence evolution.

In the space-time tensor, the turbulence field is assumed to travel with a mean reference wind speed U_{ref}. After time Δt, the field moves downstream in the positive x-direction by $U_{\mathrm{ref}}\Delta t$. Thus, for two points with a longitudinal separation of Δx, the longitudinal coherence (magnitude squared) of u component can be calculated from

$$\mathrm{coh}_{11}^2(k_1, \Delta x) = \frac{|\int \Theta_{11}(\boldsymbol{k}, \Delta x/U_{\mathrm{ref}})\mathrm{d}\boldsymbol{k}_\perp|^2}{F_1 1(k_1) F_1 1(k_1)}, \tag{15}$$

where

$$F_{11}(k_1) = \int \Phi_{11}(\boldsymbol{k})\mathrm{d}\boldsymbol{k}_\perp, \tag{16}$$

is the auto-spectrum of u component. In practice, the wavenumber based spectrum or coherence is converted to the frequency based ones using the conversion $k_1 = 2\pi f/U_{\mathrm{ref}}$, assuming the Taylor's (1938) frozen hypothesis.

2.3.2 Exponential longitudinal coherence model

On the other hand, Simley and Pao (2015) adjusted the exponential coherence model listed in the IEC 61400-1:2019 by replacing the transverse and vertical separations with longitudinal separations, which gives the following expression for the longitudinal coherence

$$\gamma_x^2(\Delta x, f) = \exp\left(-a_x \Delta x \sqrt{\left(\frac{f}{U_{\mathrm{ref}}}\right)^2 + b_x^2}\right), \tag{17}$$

where a_x and b_x are two parameters and f is the frequency. Specifically, a_x determines the decay effect of the coherence and b_x determines the intercept (value at 0 frequency) (Chen et al., 2021). Simley and Pao (2015) validated Equation (17) using LES simulations of different atmospheric stability classes. Besides, Davoust and von Terzi (2016) and Chen et al. (2021) verified the exponential evolution model using lidar measurement, showing the expression by Simley and Pao Simley and Pao (2015) agrees well with the measurement. Ih their study, they found possible a_x and b_x by fitting the coherence calculated from measurement data to the model. As a result, $0 < a_x < 6$ was observed and b_x was found in the order of magnitude $\leq 10^{-3}$.

To include the exponential longitudinal coherence model into the the analysis of lidar measurement correlation. A general "direct product" approach is used to combine the lateral-vertical coherence and the longitudinal coherence (Laks et al., 2013; Simley, 2015; Bossanyi et al., 2014; Schlipf et al., 2013a), which means the overall coherence

$$\gamma_{xyz}(f) = \gamma_{yz}(f) \cdot \gamma_x(f). \tag{18}$$

As shown by Chen et al. (2022), the "direct product" approach allows an efficient algorithm to generate Kaimal model based 4D stochastic turbulence field using statically independent 3D turbulence fields with *evoTurb*.

https://doi.org/10.5194/wes-2022-62
Preprint. Discussion started: 7 July 2022

eawe european academy of wind energy
Open Access WIND ENERGY SCIENCE DISCUSSIONS

2.4 Turbulence under different atmospheric stability

Atmospheric stability indicates the buoyancy effects on the turbulence generation and it is usually related to the temperature gradient by height. It is interesting to investigate its impact on filter design for LAC since the turbine will experience different atmospheric stability during operation. As studied by Dimitrov et al. (2017) and Peña (2019), the turbulence spectra at a given site can vary significantly with atmospheric stability. By the measurement data from the Østerild wind turbine test station in northern Denmark, Peña (2019) found that the length scale L varies significantly by different atmospheric stability classes. L is found to be the largest in unstable stability, medium in neutral stability, and the smallest in stable stability. In Figure 1, the turbulence field is generated using the 4D Mann turbulence generator (Guo et al., 2022a) with the turbulence parameters described in the caption. It is clear that a larger coherent eddy structure is observed in the unstable stability. While the eddy structure is much smaller in size under stable stability. In the neutral case, the eddy structure is somewhere between the two cases. In the rest of this paper, we use Mann turbulence parameter sets representative to unstable, neutral and stable conditions based on the study by Peña (2019) and Guo et al. (2022a), as listed in Table 1. It is worth mentioning that the $\alpha\varepsilon^{2/3}$ parameter is scaled such that the turbulence intensity corresponds to the IEC 61400-1:2019 class 1A definition.

As for the Kaimal model, we chose the parameters listed by the IEC 61400-1:2019 for the neutral stability, because these parameters were already found to give similar spectra and coherence compared to the Mann model with neutral stability parameters. Also, keeping these parameters allows readers to compare the results with that from existing literature, e.g. Schlipf (2015); Simley et al. (2018b); Dong et al. (2021). For unstable and stable stability classes, we fit the Kaimal spectra by Mann model-based spectra using the following optimization process:

$$\begin{aligned} &\min_{L_i,\sigma_i} \quad \sum_{n=1}^{N}\left[\frac{1}{k_{1,n}}\left(S_i(f_n)\cdot f_n - 2F_{ii}(k_{1,n})\cdot k_{1,n}\right)^2\right] \ , \\ &\text{s.t.} \quad k_{1,n} = \frac{2\pi f_n}{U_{\text{ref}}} \quad \text{and} \quad i = 1,2,3. \end{aligned} \tag{19}$$

Here, n is the index of the discrete frequency vector f_n and wavenumber vector $k_{1,n}$ and N is the size of the discrete vector. Note the Mann model spectra $F_{ii}(k_{1,n})$ are multiplied by 2 since they are the two-sided spectra while the Kaimal spectra are single-sided. Similarly, we fit the yz plane exponential coherence for the Kaimal model by the Mann model using

$$\begin{aligned} &\min_{a_{yz},L_c} \quad \sum_{n=1}^{N}\left[\frac{1}{k_{1,n}}\left(\gamma_{yz}(f_n) - \Re(\text{coh}_{11}(k_{1,n}))\right)^2\right] \ , \\ &\text{s.t.} \quad k_{1,n} = \frac{2\pi f_n}{U_{\text{ref}}} \quad \text{and} \quad \Delta y = \Delta z = 20\text{m}, \end{aligned} \tag{20}$$

where $\Re$ denotes the real number operator. The medium separation Δy=Δz=20m has been chosen for the optimization problem. For both optimization equations, the squared error in each discrete vector is divided by $k_{1,n}$ to ensure equivalent weighting of the optimization function at a different frequency or wavenumber ranges. The fitted spectra and yz plane coherence are shown by Figure 2(a) and (b), and the turbulence parameters are summarized in Table 1. Except for a relatively larger error for the v component auto-spectrum under very unstable stability, the rest fittings show very good agreements. It can be seen that the turbulence length scale L in Mann model Mann (1994) generally increases from very stable to unstable conditions. While the variation in the anisotropy Γ does not show a clear trend towards the atmospherically. Accordingly, the larger length scale L also leads to smaller coherence decay constant a_{yz}.

https://doi.org/10.5194/wes-2022-62
Preprint. Discussion started: 7 July 2022

eawe european academy of wind energy
Open Access WIND ENERGY SCIENCE DISCUSSIONS

Table 1. The Mann model parameters under different atmospheric stability (based on Peña (2019)) and the fitted Kaimal model parameters, with the mean wind speed of 16 ms^{-1}. $\alpha\varepsilon^{2/3}$ is scaled such that the turbulence intensity corresponds to the IEC 61400-1:2019 class 1A definition.

	Mann			Kaimal							
	$\alpha\varepsilon^{2/3}$	Γ [-]	L	L_1	L_2	L_3	σ_1	σ_2	σ_3	a_{yz} [-]	L_c
	$[\mathrm{m}^{4/3}\mathrm{s}^{-2}]$	[-]	[m]	[m]	[m]	[m]	$[\mathrm{ms}^{-1}]$	$[\mathrm{ms}^{-1}]$	$[\mathrm{ms}^{-1}]$	[-]	[m]
Unstable	0.184	140	2.6	744.8	181.9	126.4	2.82	2.34	1.98	6.5	1502.0
Neutral	0.311	49	3.1	340.2	113.4	27.72	2.82	2.25	1.41	12.0	340.2
Stable	0.652	30	2.4	101.1	33.3	27.0	2.82	2.26	1.83	13.1	101.1

Except for the spectra and yz plane coherence, Guo et al. (2022a) showed that the longitudinal coherence is related to the atmospheric stability based on measurement. In their study, a smaller intercept was found for a more stable class. Also, Simley and Pao (2015) studied the turbulence evolution under different stability classes using Large Eddy Simulations(LES) and the smaller intercept was also observed in stable atmospheric. In order to compare the longitudinal coherence under different atmospheric stability, we use three sets of $\gamma = 200, 400$, and 600 s to calculate the longitudinal coherence based on the space-time tensor $\mathbf{\Theta}$. Afterward we fit the exponential coherence (Equation 17) using the following optimization process:

$$\begin{aligned} \min_{a_x, b_x} \quad & \sum_{n=1}^{N} \left[\frac{1}{f_n} \left(\gamma_x(\Delta x, f_n) - \mathrm{coh}_{11}(f_n, \Delta x) \right)^2 \right] , \\ \text{s.t.} \quad & \Delta x = 100\mathrm{m}. \end{aligned} \tag{21}$$

Here we chose to fit the separation at $\Delta x = 100\mathrm{m}$, which is the medium separation for a commercial lidar measuring in front of the turbine. The fitted coherence is shown in Figure 2(c). The fitted exponential coherence parameters a_x and b_x are summarized in Table 2, and they show similar trend as the observation by Simley and Pao (2015) using LES. For an unstable atmosphere, a_x is generally larger and b_x is in a very small order close to 0. In neutral condition, a_x lies in a medium value and b_x is also a small order close to 0. As for the stable case, the a_x is the smallest meaning a weaker coherence decay while the b_x is larger and results in a smaller intercept.

Table 2. The fitted parameters for the exponential longitudinal coherence model.

Stability		γ = 200 s	γ = 400 s	γ = 600 s
Unstable	a_x	8.2	5.1	4.1
	b_x	8.52×10^{-5}	8.02×10^{-5}	7.67×10^{-5}
Neutral	a_x	2.9	1.8	1.4
	b_x	1.59×10^{-4}	1.49×10^{-4}	1.42×10^{-4}
Stable	a_x	1.6	1.0	0.8
	b_x	9.18×10^{-4}	8.59×10^{-4}	8.27×10^{-4}

https://doi.org/10.5194/wes-2022-62
Preprint. Discussion started: 7 July 2022

eawe european academy of wind energy
Open Access WIND ENERGY SCIENCE DISCUSSIONS

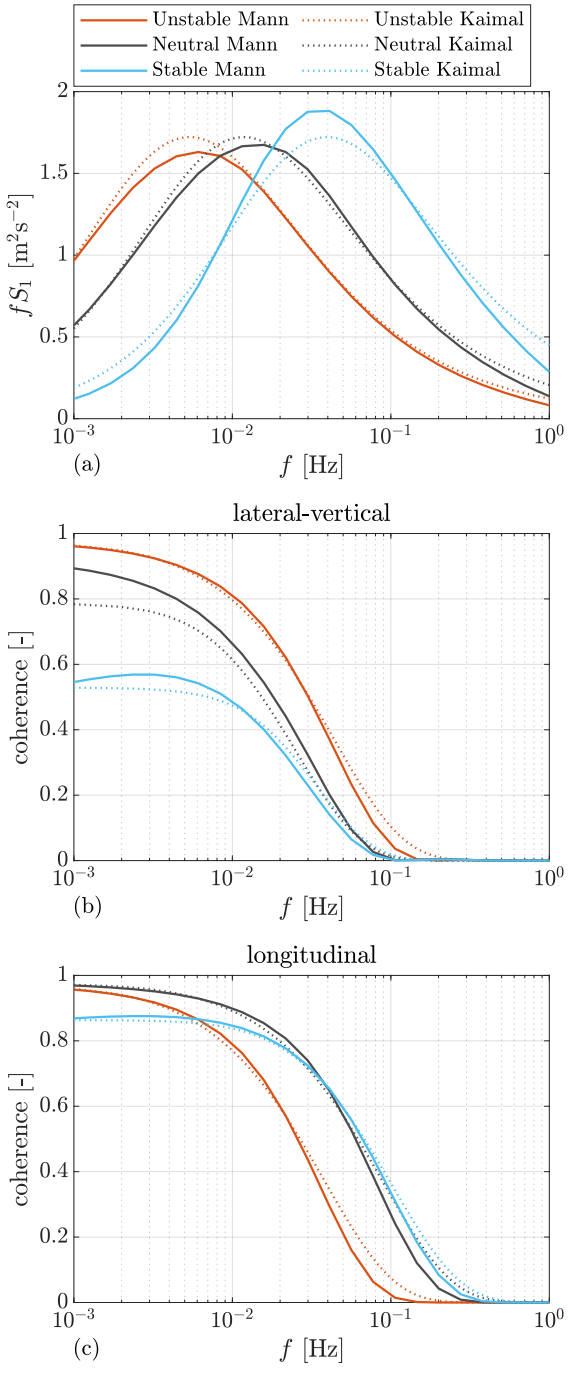

Figure 2. (a) The auto-spectra of the longitudinal velocity component under different stability classes. (b) Lateral-vertical coherence of the longitudinal velocity component calculated using the Mann spectral tensor and fitted by the exponential coherence model. Note the co-coherence is shown for the Mann spectral tensor. (c) Longitudinal coherence of the longitudinal velocity component calculated using the space-time tensor and fitted by the exponential coherence model.

https://doi.org/10.5194/wes-2022-62
Preprint. Discussion started: 7 July 2022

eawe european academy of wind energy
Open Access WIND ENERGY SCIENCE DISCUSSIONS

Based on the study by Guo et al. (2022a), γ was found to be 430 s and 207 s for neutral and stable stability classes respectively, while the τ in unstable case has not been derived due to lack of samples from measurement. Since $\gamma = 200$ s or 400 s gives a rarely large a_x based on existing literature (see Chen et al. (2021)), we decided to chose $\gamma = 600$ s for the unstable condition. And $\gamma = 400$ and $\gamma = 200$ are used for neutral and stable stability classes.

3 Correlation between lidars and turbines

In this section, the rotor effective wind speed, the REWS estimated by lidar will first be discussed. Then the auto-spectra of these two signals and the cross-spectrum between them will be presented. In the end, we summarize the lidar wind preview quality for the investigated four-beam lidar and the NREL 5.0MW reference turbine under different atmospheric stability classes.

3.1 Turbine-estimated rotor effective wind speed

As discussed by Schlipf (2015), one way of defining the turbine estimated rotor effective wind speed for control purpose is the mean longitudinal component over the rotor area:

$$u_{\mathrm{RR}}(x) = \frac{1}{\pi R^2} \int_D u_1(\boldsymbol{x}) \mathrm{d}y \mathrm{d}z. \tag{22}$$

where D denotes the integration over the rotor area defined by rotor radius R.

For Mann model, as derived by Held and Mann (2019), the auto-spectrum of the REWS u_{RR} can be calculated using the spectral tensor by

$$S_{\mathrm{RR}}(k_1) = \int_{-\infty}^{\infty} \Phi_{11}(\boldsymbol{k}) \frac{4J_1^2(\kappa R)}{\kappa^2 R^2} \mathrm{d}k_2 \mathrm{d}k_3, \tag{23}$$

with $\kappa = \sqrt{k_2^2 + k_3^2}$ and J_1 the Bessel function of the first kind. The detailed derivation of the auto-spectrum can be found in Held and Mann (2019); Mirzaei and Mann (2016).

As for Kaimal model, the spectrum is derived by Schlipf et al. (2013a); Schlipf (2015), i.e.

$$S_{\mathrm{RR}}(f) = \frac{S_1(f)}{n_{\mathrm{R}}^2} \sum_{i=1}^{n_{\mathrm{R}}} \sum_{j=1}^{n_{\mathrm{R}}} \gamma_{yz}(\Delta yz_{ij}, f), \tag{24}$$

where Δyz_{ij} is the the separation distance between pint i and j in the same yz plane, and n_{R} is the total number of points in the rotor area. The detailed derivation of the auto-spectrum can be found in Schlipf (2015).

3.2 Lidar-estimated rotor effective wind speed

Lidar utilizes the Doppler spectrum contributed by the aerosol backscatters within the probe volume to determine wind measurement. It is necessary to include the probe volume averaging effect. Mann et al. (2009) shows that the lidar line-of-

https://doi.org/10.5194/wes-2022-62
Preprint. Discussion started: 7 July 2022

eawe european academy of wind energy
Open Access WIND ENERGY SCIENCE DISCUSSIONS

sight(LOS) measurements at a focus position $\boldsymbol{x} = (x, y, z)$ can be approximated by

$$v_{\mathrm{los}}(\boldsymbol{x}) = \int_{-\infty}^{\infty} \varphi(r)\boldsymbol{n} \cdot \boldsymbol{u}(r\boldsymbol{n} + \boldsymbol{x})\mathrm{d}r. \tag{25}$$

where $\boldsymbol{n} = (n_1, n_2, n_3) = (\cos\beta\cos\phi, \cos\beta\sin\phi, \sin\beta)$ is a unit vector align in the direction of a lidar beam that can be simply calculated after knowing the azimuth angle ϕ and elevation angle β. r is the displacement along the lidar beam direction from the focused position $\boldsymbol{x}$. $\varphi(r)$ is the weighting function due to the lidar volume averaging. In this work, a typical pulsed lidar is considered whose weighting function is modeled by a Gaussian-shape function (Schlipf, 2015)

$$\varphi(r) = \frac{1}{\sigma_{\mathrm{L}}\sqrt{2\pi}}\exp(-\frac{r^2}{2\sigma_{\mathrm{L}}^2}) \quad \text{with} \quad \sigma_{\mathrm{L}} = \frac{W_{\mathrm{L}}}{2\sqrt{2\ln 2}}, \tag{26}$$

where the full width at half maximum W_{L} is about 30 m.

Since lidar only provides the wind speed in the LOS direction, the u component is needed to be reconstructed from LOS speed. A simple algorithm is to assume zero v and w components because they usually contribute much less than the u component on the LOS speed. In fact, this is true if lidar beam misalignment to the longitudinal direction is small. Based on this assumption, the lidar estimated rotor effective wind speed is often obtained by (see Schlipf (2015))

$$u_{\mathrm{LL}}(t) = \frac{1}{n_{\mathrm{b}}\cos\beta\cos\phi}\sum_{i=1}^{n_{\mathrm{b}}} v_{\mathrm{los},i}(t), \tag{27}$$

where n_{b} is total number of lidar beams and $v_{\mathrm{los},i}(x)$ denotes the ith lidar measurement.

Guo et al. (2022a) suggested to calculate the auto-spectrum of the lidar estimated REWS (u_{LL}) from the Mann model extended space-time tensor by

$$\begin{aligned} S_{\mathrm{LL}}(k_1) = &\frac{1}{(n_{\mathrm{b}}\cos\beta\cos\phi)^2}\sum_{i,j=1}^{n_{\mathrm{b}}}\sum_{l,m=1}^{3}\int n_{il}n_{jm}\Theta_{lm}(\boldsymbol{k}, \Delta t_{ij}) \\ &\exp(\mathrm{i}\boldsymbol{k}\cdot(\boldsymbol{x}_i - \boldsymbol{x}_j))\hat{\varphi}(\boldsymbol{k}\cdot\boldsymbol{n}_i)\hat{\varphi}(\boldsymbol{k}\cdot\boldsymbol{n}_j)\mathrm{d}\boldsymbol{k}_{\perp}, \end{aligned} \tag{28}$$

where $\boldsymbol{x}_i$ and $\boldsymbol{n}_i$ denote the focus position vector and the unit vector of the ith lidar measurement respectively, n_{il} is the lth element in the unit vector $\boldsymbol{n}_i$, and

$$\hat{\varphi}(\nu) = \int_{-\infty}^{\infty}\varphi(r)\exp(-i\nu r)\mathrm{d}r = \exp(-\nu^2\frac{\sigma_{\mathrm{L}}^2}{2}) \tag{29}$$

is the Fourier transform (non-unitar convention) of the weighting function of lidar, and $\Delta t_{ij} = (x_i - x_j)/U_{\mathrm{ref}}$ is the time required for turbulence to propagates from position x_i to x_j. A more detailed derivation of Equation (28) can be found in Mirzaei and Mann (2016); Held and Mann (2019); Guo et al. (2022a).

For Kaimal model, the auto-spectrum can be derived based on the Fourier transform:

$$\begin{aligned} S_{\mathrm{LL}}(f) &= \mathcal{F}\{u_{\mathrm{LL}}\}\mathcal{F}^*\{u_{\mathrm{LL}}\} \\ &= \frac{1}{(n_{\mathrm{b}}\cos\beta\cos\phi)^2}\sum_{i,j=1}^{n_{\mathrm{b}}}\mathcal{F}\{v_{\mathrm{los},i}\}\mathcal{F}^*\{v_{\mathrm{los},j}\}, \end{aligned} \tag{30}$$

https://doi.org/10.5194/wes-2022-62
Preprint. Discussion started: 7 July 2022

eawe european academy of wind energy
Open Access WIND ENERGY SCIENCE DISCUSSIONS

where $\mathcal{F}\{\ \}$ denotes the Fourier transform. The Fourier transform of the ith LOS speed $v_{\mathrm{los},i}$ is quite lengthy thus is not extended here. The detailed expression can be found in Chen et al. (2022).

3.3 Cross-spectrum between rotor and lidar

When turbulence evolution is considered with Mann model, Guo et al. (2022a) shows that the cross-spectrum between REWS u_{RR} and the lidar estimated one u_{LL} can be calculated using the space-time tensor by

$$S_{\mathrm{RL}}(k_1) = \frac{1}{n_{\mathrm{b}}\cos\beta\cos\phi}\sum_{i=1}^{n_{\mathrm{b}}}\sum_{j=1}^{3}\int n_{ij}\Theta_{j1}(\boldsymbol{k},\Delta t_i)\,\hat{\varphi}(\boldsymbol{k}\cdot\boldsymbol{n}_i)\exp(\mathrm{i}\boldsymbol{k}\cdot\boldsymbol{x}_i - k_1\Delta x_i)\frac{2J_1(\kappa R)}{\kappa R}\mathrm{d}\boldsymbol{k}_\perp, \tag{31}$$

where, Δx_i is the longitudinal separation between the rotor plane and the ith lidar measurement position and $\Delta x_i = x_i - x_{\mathrm{R}} = x_i$. Because the rotor plane is often defined at $x_{\mathrm{R}} = 0$ m. Δt_i is the time required for the turbulence field to move from the ith lidar measurement position to the rotor plane, which can be approximated by $\Delta t_i = |\Delta x_i|/U_{\mathrm{ref}}$.

Similarly, following Schlipf (2015), the cross-spectrum for Kaimal model is

$$\begin{aligned} S_{\mathrm{RL}}(f) &= \mathcal{F}\{u_{\mathrm{RR}}\}\mathcal{F}^*\{u_{\mathrm{LL}}\} \\ &= \frac{1}{n_{\mathrm{b}}n_{\mathrm{R}}\cos\beta\cos\phi}\sum_{i=1}^{n_{\mathrm{R}}}\sum_{j=1}^{n_{\mathrm{b}}}\mathcal{F}\{u_i\}\mathcal{F}^*\{v_{\mathrm{los},j}\}, \end{aligned} \tag{32}$$

with u_i the ith longitudinal wind component in the rotor swept area. See Chen et al. (2022). for detailed derivation of the Fourier transform of $v_{\mathrm{los},j}$, where the main algorithm is to loop over the Fourier transform of all velocity components included in u_i and $v_{\mathrm{los},j}$.

3.4 Lidar wind preview and filter design: case analysis

To evaluate the preview quality of lidar measurement, one can calculate the lidar-rotor coherence by

$$\gamma_{\mathrm{RL}}(f) = \frac{|S_{\mathrm{RL}}(f)|^2}{S_{\mathrm{RR}}(f)S_{\mathrm{LL}}(f)}. \tag{33}$$

Then, a measurement coherence bandwidth (the wavenumber at which the coherence drops to 0.5, noted as $k_{0.5}$) can be found. Note that $k_{0.5} = 2\pi f_{0.5}/U_{\mathrm{ref}}$ where $f_{0.5}$ is the frequency at which the coherence drops to 0.5. $k_{0.5}$ is usually used as the optimization criteria for the LAC-oriented lidar measurement trajectory Schlipf et al. (2018a).

In this work, we chose the medium-size NREL 5MW reference wind turbine with a rotor diameter of 126 m (Jonkman et al., 2009) and a typical four-beam pulse lidar trajectory. The lidar trajectory is firstly optimized following the method proposed by Schlipf et al. (2018a) using the space-time tensor-based lidar-rotor coherence γ_{RL}. The turbulence parameters corresponding to the neutral stability in Table 1 are considered in the optimization process. The optimized trajectory of the used lidar is given in Table 3. A front view of the lidar and turbine geometry is shown in Figure 3.

https://doi.org/10.5194/wes-2022-62
Preprint. Discussion started: 7 July 2022

eawe european academy of wind energy
Open Access WIND ENERGY SCIENCE DISCUSSIONS

With the optimized lidar trajectory, we show the coherence γ_{RL} under different stability classes in Figure 4 (a). It can be seen that the coherence using Mann model-based space-time tensor is generally better than that using the Kaimal model. For both models, the coherence in neutral and stable stability classes is higher than that in the unstable stability which can be caused by stronger turbulence evolution in the unstable situation. The coherence in the unstable case is especially lower using the Kaimal model, which can be caused by the direct product method. Based on the investigation by Simley (2015) using LES, combing coherence using the direct product can underestimate the overall coherence.

Except for the coherence, another indicator of how well the lidar predict the REWS can be the following transfer function (Schlipf, 2015; Simley and Pao, 2013)

$$|G_{\mathrm{RL}}(f)| = \frac{|S_{\mathrm{RL}}(f)|}{S_{\mathrm{LL}}(f)}. \tag{34}$$

If a filter with the gain $G_{\mathrm{RL}}(f)$ turns out to be an optimal Wiener filter (Simley and Pao, 2013; Wiener et al., 1964), which results in minimal output variance for a multi-inputs multi-outputs system. At a certain frequency, the larger gain means that less information needs to be filtered out before the signal is used. So, it indicates how much information measured by the lidar is usable for feed-forward control.

Table 3. Parameters of the optimal four-beam pulsed lidar system. Optimized according to the measurement coherence bandwidth using the space-time tensor model.

Parameters	Values	Units
Number of beams	4	[-]
Beam azimuth angles	14.4, 14.4, -14.4, -14.4	[°]
Beam elevation angles	14.0, -14.0, -14.0, 14.0	[°]
Range gates in x	50 to 170	[m]
Range gates step in x	13.3	[m]
Sampling frequency	1.0 (each beam)	[Hz]
Full width at half maximum	30	[m]

The transfer functions under the three investigated stability classes are shown by Figure 4 (b). The transfer function gains are similar in the three stability classes for the space-time tensor-derived results. As for the results by the Kaimal model, the transfer function gain is lower in the unstable stability but similar in natural and stable stability classes.

By the turbulence spectral model, which represents the mean spectral properties, we can obtain the expected Wiener transfer function gain. However, in real operation, the Wiener filter design is more complicated and requires a higher-order filter. In contrast, a linear filter that has similar damping as the Wiener filter can also provide a similar filtering effect as the Wiener filter. The linear filter is usually designed to have a cutoff frequency at -3 dB of the Wiener filter (Schlipf, 2015; Simley et al., 2018a). A list of the cutoff frequency by fitting the G_{RL} in Figure 4 (b) are provided in Table 4. The cutoff frequencies by the Mann model-based space-time tensor are generally larger than that by the Kaimal model. For the same turbulence model,

https://doi.org/10.5194/wes-2022-62
Preprint. Discussion started: 7 July 2022

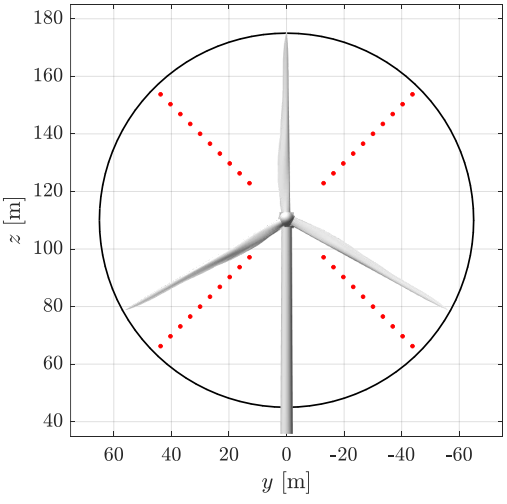

Figure 3. A front view of the NREL 5.0 MW turbine and the optimized four-beam trajectory.

the resulting cut-off frequency does not change significantly to the analyzed turbulence stability conditions. It can be seen that the turbulence parameters of different atmospheric stability classes do not influence the cutoff frequency very much and the difference lies in the order of 10^{-3}. This also indicates that the filter design is not sensitive to the change in turbulence parameters related to atmospheric stability and a constant filter design is robust. In the rest of this work, we will use the constant cut-off frequency derived from neutral stability for both the Mann model-based and the Kaimal model-based simulations. For example, the 0.0490 Hz and 0.0449 Hz will be used respectively for the Mann model and the Kaimal model-based simulations with a mean wind speed of 16 ms^{-1}.

Table 4. The cutoff frequency corresponds to -3 dB at the G_{RL} magnitude. Calculated with a mean wind speed of 16 ms^{-1}.

	Mann	Kaimal
Unstable	0.0544	0.0347
Neutral	0.0490	0.0449
Stable	0.0455	0.0439

4 Lidar-assisted controller design

In this section, we introduce the lidar-assisted turbine controller theory and its integration to OpenFAST aeroelastic simulation.

https://doi.org/10.5194/wes-2022-62
Preprint. Discussion started: 7 July 2022

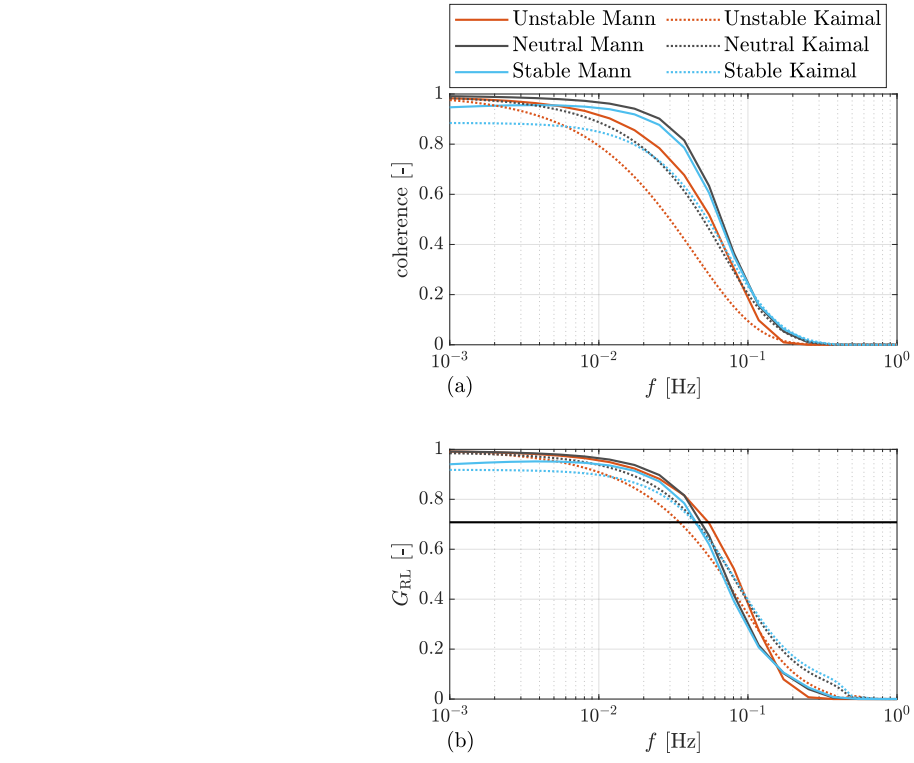

Figure 4. (a) Coherence between lidar estimated RWES and the turbine based REWS. (b) The optimal transfer function gain. The black dot line corresponds to the -3dB magnitude.

4.1 Data exchange framework

To configure LAC in the OpenFAST aeroelastic simulation, we chose to use the Blade style interface DNV-GL (2016). The interface is responsible for exchanging variables between the OpenFAST executable and the external controllers compiled as Dynamic Link Library(DLL). To make each controller module as standard alone as possible, we programmed an open-source main DLL (written in FORTRAN), namely the “wrapper DLL". The main function of the wrapper DLL is to call the sub-DLLs by a specified sequence. Note all the sub-DLLs work based on the same variable exchange pattern specified by the Bladed style interface. This means each sub-DLL can also be called by OpenFAST independently and directly. Or, several sub-DLLs can be called by the wrapper DLL together. An overview of the LAC and OpenFAST interface is shown by Figure 5. Three sub-DLLs will be called by the wrapper DLL following the sequence from up to below in the figure.

https://doi.org/10.5194/wes-2022-62
Preprint. Discussion started: 7 July 2022

eawe european academy of wind energy
Open Access WIND ENERGY SCIENCE DISCUSSIONS

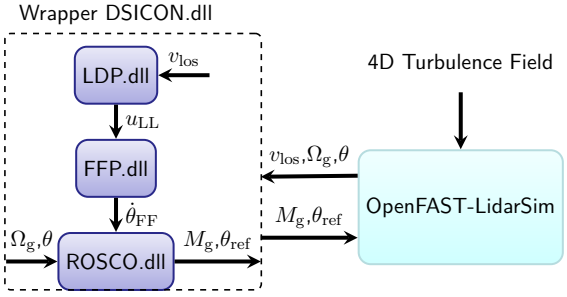

Figure 5. The overall OpenFAST and LAC interface. LDP: Lidar Data Processing. FFP: Feedforward Pitch. ROSCO: the reference FB controller.

4.2 Lidar data processing

As mentioned before, the lidar measurement data needs to be processed before it can be used for control. The first sub-DLL is the Lidar Data Processing (LDP) which calculates the lidar estimated REWS from the lidar LOS speed.

In reality, the lidar usually does not measure all beam directions simultaneously, thus a time-averaging window needs to be applied. For the four-beam lidar used in this work, the averaging window is chosen to be 1s which is the time required to finish a full scan by four beams. To apply the averaging window, the LDP module also needs to record the leading time of the successful measurement. The leading time can be approximated by $\Delta x_i / U_{\mathrm{ref}}$. When estimating the REWS, only the LOS measurements whose leading times are within the time averaging window will be chosen and then Equation (27) is applied to estimate REWS. Besides, the blockage effect is considered in the simulation and this phenomenon is included in the updated OpenFAST lidar module Guo et al. (2022b). Due to the blade blockage, the LOS measurements for a certain lidar beam are not always available. Therefore, the LDP module estimates the REWS only using all the available LOS measurements.

4.3 Feedback only controller

A typical variable-speed wind turbine is controlled by a blade pitch and generator torque controller. A baseline collective feedback blade pitch control is achieved by a proportional-integral (PI) controller Jonkman et al. (2009):

$$\theta_{\mathrm{FB}} = k_{\mathrm{p}}(\Omega_{\mathrm{g}} - \Omega_{\mathrm{g,ref}}) + \frac{k_{\mathrm{p}}}{T_{\mathrm{I}} s}(\Omega_{\mathrm{g}} - \Omega_{\mathrm{g,ref}}) \tag{35}$$

where θ_{FB} is the feedback pitch reference value. $\Omega_{\mathrm{g,ref}}$ is the generator speed control reference, k_{p} the proportional gain, T_{I} the integrator time constant, and s is the complex frequency. The pitch controller is only active above-rated wind speed, and k_{p} and T_{I} are scheduled to have a constant closed-loop behavior through gain scheduling Abbas et al. (2022). For the NREL 5.0 MW wind turbine, the desired damping and angular frequency are tuned to be 0.7 and 0.5 rads^{-1}, respectively.

For better code accessibility, the recently developed open-source reference controller: ROSCO (v2.4.0) by Abbas et al. (2022) is used as the reference FB-only controller. ROSCO uses PI controller for the pitch control in the above-rated wind speed operation. In terms of torque control in the above-rated operation, we have chosen the option of constant power mode

https://doi.org/10.5194/wes-2022-62
Preprint. Discussion started: 7 July 2022

in our simulations. See (Abbas et al., 2022) for a more detailed description of the reference controller. We have modified the ROSCO source code to allow it to accept the feedforward pitch rate signal. The feedforward pitch rate (see next section) is added before the integrator of the PI controller.

4.4 Combined feedforward and feedback controller

The collective feedforward pitch control proposed by Schlipf (2015) is used in this work where the feedforward pitch reference value is obtained by

$$\theta_{\mathrm{FF}} = u_{\mathrm{LLf}} \frac{\mathrm{d}\theta_{\mathrm{ss}}}{\mathrm{d}u_{\mathrm{RR}}} \tag{36}$$

with u_{LLf} the filtered REWS estimated by lidar and $\frac{\mathrm{d}\theta_{\mathrm{ss}}}{\mathrm{d}u_{\mathrm{RR}}}$ the derivative of steady-state pitch angle θ_{ss} with respect to u_{RR}. Figure 6 shows the general control diagram with the lidar-assisted pitch forward signal θ_{FF}. In practice, the pitch time derivative of the pitch forward signal is fed into the integral block of the feedback PI controller. This gives the overall collective pitch control reference as

$$\theta_{\mathrm{ref}} = \theta_{\mathrm{FB}} + \frac{1}{s}\dot{\theta}_{\mathrm{FF}}. \tag{37}$$

A Feedforward Pitch (FFP) sub-DLL is programmed to be responsible for filtering the lidar estimated REWS and provide forward pitch rate at correct time. A first order low pass filter with the following transfer function

$$\frac{2\pi f_{\mathrm{c}}}{s + 2\pi f_{\mathrm{c}}}, \tag{38}$$

where f_{c} is the cut-off frequency, is applied to filter the u_{LL} signal. Based on the filter cutoff frequency, the time delay introduced by the filtering can be estimated and the pitch forward signal is send to ROSCO after accounting for the pitch actuator delay. Basically, the signal that fulfills

$$t_{\mathrm{lead}} - t_{\mathrm{filter}} - t_{\mathrm{pitch}} = 0, \tag{39}$$

is activated.

5 Simulation, results and discussion

In this section, we use the open-source aeroelastic simulation tool OpenFAST to further evaluate the benefits of LAC. The simulation results will be presented and discussed.

5.1 Simulation environment

5.1.1 Lidar simulation

Previously, the OpenFAST (v3.0) has been modified to integrate a lidar simulation module (Guo et al., 2022b). The lidar simulation module includes several main characteristics of nacelle lidar measurement: 1) lidar probe volume, 2) turbulence

https://doi.org/10.5194/wes-2022-62
Preprint. Discussion started: 7 July 2022

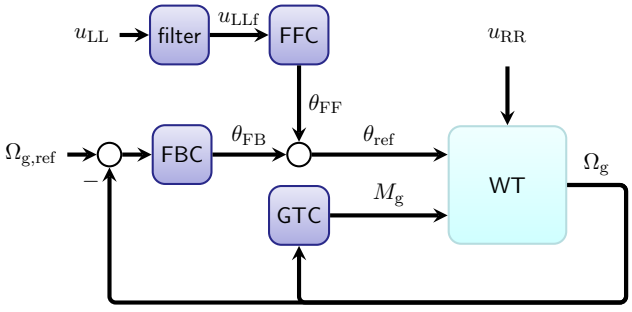

Figure 6. The overall control diagram. FFC: feedforward pitch controller, FBC: collective feedback pitch controller, GTC: generator torque controller. Note that the real time pitch angle (θ) signal is also used in the FBC and GTC for controller scheduling.

evolution (lidar measures at the upstream wind field), 3) the LOS speed contributed by nacelle motion, 4) lidar beam blockage by turbine blade and 5) adjustable measurement availability. Based on the study by (Guo et al., 2022b) the blade blockage does not have an impact on the lidar measurement coherence for above rated wind speed operation, but special treatment needs to be made to process the invalid measurement caused by blade blockage effect. In this work, the similar algorithm discussed by (Guo et al., 2022b) is used to process the invalid measurement data. Also, the data unavailability caused by low back-scatters are not considered. Therefore, the unavailable data is only caused by the blade blockage.

5.1.2 Stochastic turbulence generation

To include the turbulence evolution for the aeroelastic simulation. Four-dimensional stochastic turbulence field is required. We use the newly developed *4D-Mann-Turbulence-Generator* (Guo et al., 2022a) and *evoturb* (Chen et al., 2022) to generate Mann model and Kaimal model -based 4D turbulence fields respectively. The turbulence parameters representative for three atmospheric stability classes are used (see Table 1 in Section 2).

For *4D Mann turbulence generator*, since the generated turbulence only contains the fluctuation part of the turbulence, we add the mean field (only for u component) considering a power law shear profile with a shear exponent of 0.2. Each 4D turbulence field has a size of $4096 \times 11 \times 64 \times 64$ grid points, corresponding to the time, and the x, y and z directions. The lengths in the y and z directions are both 310 m, which is much larger than the rotor size. The reason of choosing this size is to avoid the periodicity of the turbulence field in y and z directions (1998).

For Kaimal model-based 4D wind field. *evoTurb* is used which calls *Turbsim* (Jonkman, 2009) to generated statistically independent 3D turbulence field and then composite 4D turbulence with the exponential longitudinal coherence discussed in Section 2. Only the coherence of u component is considered and the rest velocity components are not correlated. Each turbulence field has a size of $4096 \times 11 \times 31 \times 31$ grid points, corresponding to the time, and the x, y and z directions. The lengths in the y and z directions are both 150 m.

For both types of 4D turbulence fields, the hub height mean wind speed from 14 ms^{-1} to 24 ms^{-1} with a step of 2 ms^{-1} are considered. The turbulence parameters are chosen based on Table 1. However, $\alpha\varepsilon^{2/3}$, σ_1, σ_2, and σ_3 are adjusted according the

https://doi.org/10.5194/wes-2022-62
Preprint. Discussion started: 7 July 2022

the mean wind to reach the turbulence intensity corresponding to class 1A, as specified in IEC 61400-1:2019. The positions in the x direction both contain the rotor plane position and the lidar range gate positions (see Table 3). Taylor's (1938) Frozen theory is applied within the probe volume, which has been shown not to influence the lidar measurement spectral properties by Chen et al. (2022). For example, the lidar measurement gate at $x = 50$ m is calculated using the yz plane wind field at $x = 50$ m which is shifted with Taylor's Frozen theory to count for the lidar probe volume averaging. The time length of each field is 2048 s which is close to a 30 min simulation.

5.1.3 Simulation setup

For each stability class, we generate 4D turbulence fields with 12 different rand seed numbers. For each turbulent wind field, the OpenFAST simulation is executed with the following configurations: 1) FB control using ROSCO only; 2) FFFB (feedforward+feedback) control using lidar measurements. All the degree-of-freedoms for a fixed bottom turbine except for the yawing are activated. For each simulation result, we remove the initial 100 s simulation which contains the initialization.

5.2 Results and discussion

5.2.1 Time series

In Figure 7, we take the one simulation using 4D Mann turbulence with the neutral stability condition as an example to show the time series.

Panel (a) compares the REWS estimated by the lidar data processing algorithm and that estimated by the extended Kalman filter (EKF) (Julier and Uhlmann, 2004) implemented in ROSCO. The lidar estimated REWS is shifted according to the time buffer by the FFP module so that it does not show any time lag in the plot. The lidar estimated REWS shows good agreement with that estimated by the Karmann filter. It can be seen that some additional fluctuations with higher frequency appear in the time series of ROSCO-based REWS. This can be caused by the fact that ROSCO only uses one degree-of-freedom model containing the rotor rotational motion and all the other structural motions affecting the rotor speed can be "mistakenly". estimated as wind speed.

Panel (b) shows that the rotor speed obviously fluctuates less using FFFB control compared to that using FB control only. Also, the peak values with FFFB control are less severe.

The tower fore-aft bending moments are compared in panel (c), where the tower bending moment (M_{yT}) is generally less fluctuating with the help of FFFB control. Further, the blade root out-of-plane bending moment ($M_{\mathrm{y,root}}$) is shown by the panel (d), in which the difference between FFFB slightly reduces the fluctuation compared to FB control only. The low-speed shaft torques (M_{LSS}) are compared in panel (e). Again it is clear that the fluctuation with FFFB control is a bit lower than that with FB-only control.

In panel (f), we show the pitch action between the two control strategies. The pitch angles in the FFFB control generally lead that by the FB control in time, as expected. The pitch angle trajectory is overall similar between FFFB control and FB control only.

https://doi.org/10.5194/wes-2022-62
Preprint. Discussion started: 7 July 2022

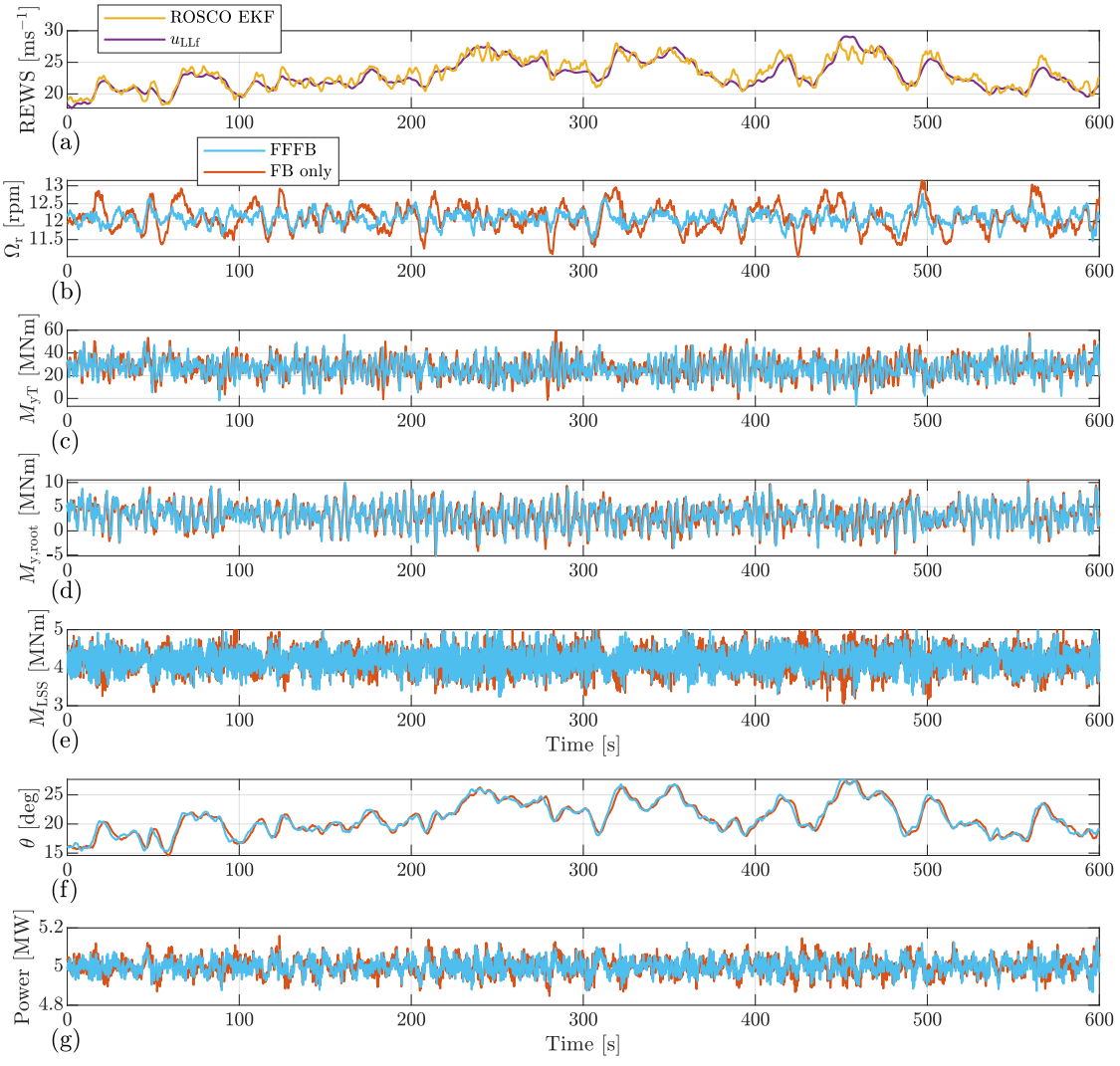

Figure 7. The time series collected from OpenFAST simulation. The case with Mann model and neutral stability parameters is shown. Note the same 3D wind field (y, z, t) is applied to the rotor when performing simulations with the FFFB control and the FB only control. Simulated with a mean wind speed of 16 ms^{-1}.EKF: extended Kalman filter.

Lastly, the generator power is shown in panel (g) where much less power fluctuation is observed in FFFB control. Because the power fluctuation is highly coupled with the rotor speed fluctuation, the less fluctuating power can be expected from the less rotor speed fluctuation in FFFB control.

https://doi.org/10.5194/wes-2022-62
Preprint. Discussion started: 7 July 2022

eawe european academy of wind energy
Open Access WIND ENERGY SCIENCE DISCUSSIONS

5.2.2 Spectral Analysis

We estimate the spectra from the collected time series using Welch's (1967) method. The spectra are averaged by different samples corresponding to the simulated results by different random seed numbers.

Before comparing the OpenFAST outputs spectra, the spectra of the REWS by the input turbulent wind fields are first compared in Figure 8. Here, the simulated REWS is calculated by averaging the u components within the rotor swept area from the discrete turbulent wind field. We show that the simulated spectra follow well with the theoretical one, which validates the turbulence simulation. In Section 2, the single point u component spectrum by the two models is fitted. Also, the yz plane coherence is fitted using a single separation. Here, it can be seen that the REWS spectra by two models show a similar trend in different atmospheric stability classes. In the unstable case, the RWES spectrum does not reduce a lot compared to a single point u spectrum in Figure 2 and the spectrum peak appears at a lower frequency. Because the turbulence field has a more large-scale coherent structure as depicted by Figure 1. In the stable case, everything is opposite to the unstable case where the REWS spectrum is much lower compared to the single point u spectrum, because of the low-level coherence and the spatial filtering effect of the rotor. In addition, the neutral stability shows a medium spatial filtering effect and the spectrum peak is between that of unstable and stable conditions. For each stability class, it can be seen that the Kaimal-derived REWS generally has a lower spectrum compared to that derived by the Mann model. This can be caused by the fact that the yz plane coherence by the Mann model is more complicated than the exponential coherence model used in the Kaimal model. Fitting the coherence using one separation is insufficient to represent all possible separations.

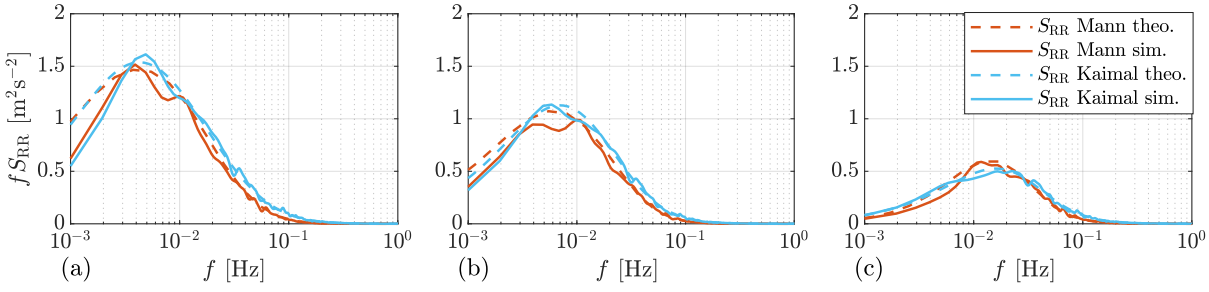

Figure 8. The auto-spectra of REWS. "theo.": theoretical spectra by the models discussed in Section 3, i.e. Equation (23) and (24). "sim.": the spectra estimated from the time series of the turbulent wind fields in OpenFAST simulations, using Welch's (1967) method. The results with a mean wind speed of 16 ms^{-1} is considered.

In Figure 9 and Figure 10, the auto-spectra of some of the most interested output variables by FB only control and FFFB control are compared. Figure 9 shows the results using Mann model and Figure 10 shows the result by Kaimal model.

Panel (a), (b), and (c) compare the rotor speed spectra between FFFB control and FB control under three stability classes. The FFFB control generally reduces the rotor speed spectrum in the frequency range from 0.01 to 0.1 Hz. It can also be seen that the spectra using the Mann model and Kaimal model show some differences, which can be summarized as higher spectra

https://doi.org/10.5194/wes-2022-62
Preprint. Discussion started: 7 July 2022

in the rotor motion by the Kaimal model than the Mann model. However, the spectra by the Mann model and Kaimal model generally have similar shapes.

The comparison of tower fore-aft bending moment is shown by the panel (d), (e), and (f). In neutral and stable cases, the main benefits bought by FFFB control are the reductions in the frequency range from 0.01 Hz to 0.2 Hz, which is as expected, since the lidar-rotor transfer function becomes zero at 0.2 Hz. Below 0.01 Hz, there are not many differences between FB only and FFFB controls, because the tower fore-aft mode is naturally damped well in this frequency range.

Panel (g), (h), and (i) show the blade root out-of-plane moment of blade 1. The reduction in the blade root out-of-plane moment is not very observable from the plots, because the spectrum is mainly composited by the excitation at 1p frequency.

The comparison of low-speed shaft torque is shown by the panel (j), (k), and (l). Using FFFB control brings some benefits in the frequency range from 0.01 to 0.1 Hz which is similar to the reduction range of the rotor speed.

Overall, the relative reductions in the spectra bought by adding FF control mainly lie in the frequency range where the lidar-rotor transfer function is above zero. For very low-frequency ranges, the turbine motions are naturally damped thus no benefits are brought by adding the pitch forward signal. Based on the spectral analysis, we found reductions mainly in rotor speed, part in tower fore-aft moment, and slightly in low-speed shaft torque. Also, the reductions are observed by both turbulence models in three different atmospheric stability classes.

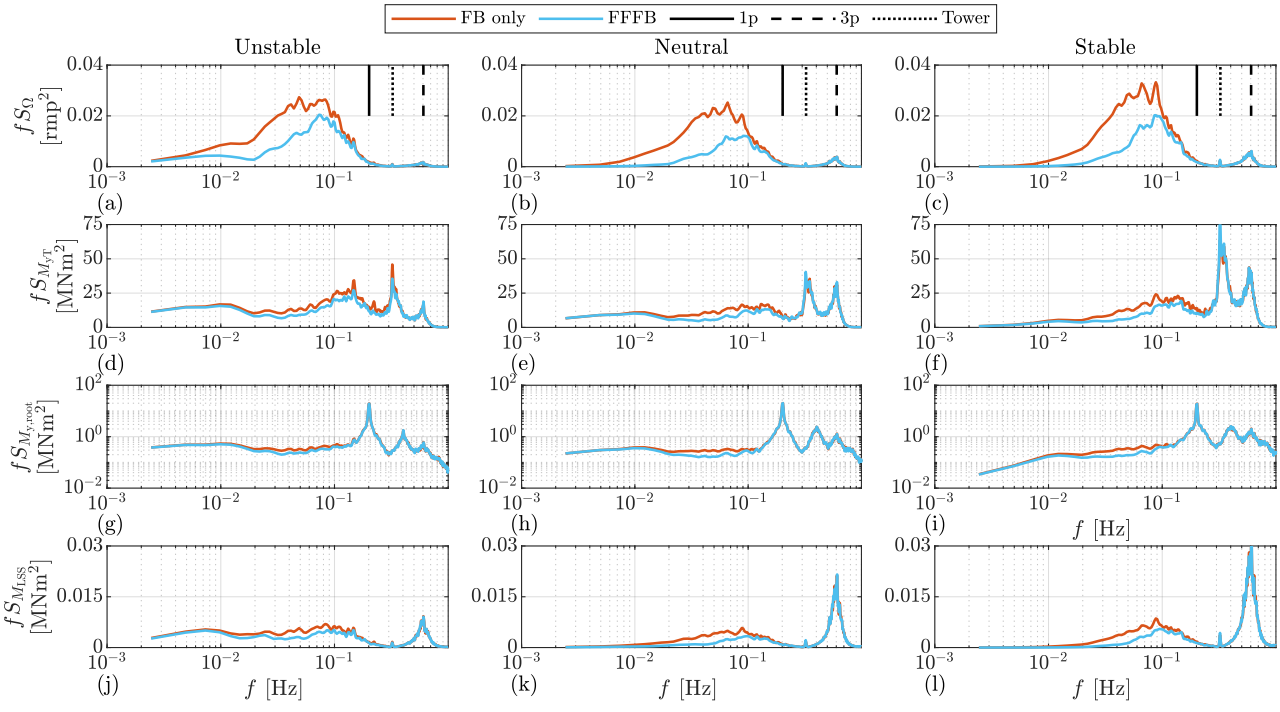

Figure 9. The auto-spectra estimated from OpenFAST output time series. The simulation results are obtained using Mann model. The mean wind speed is 16 ms^{-1}. Note that the y axis of the blade root bending moment is set to logarithmic for better readability.

https://doi.org/10.5194/wes-2022-62
Preprint. Discussion started: 7 July 2022

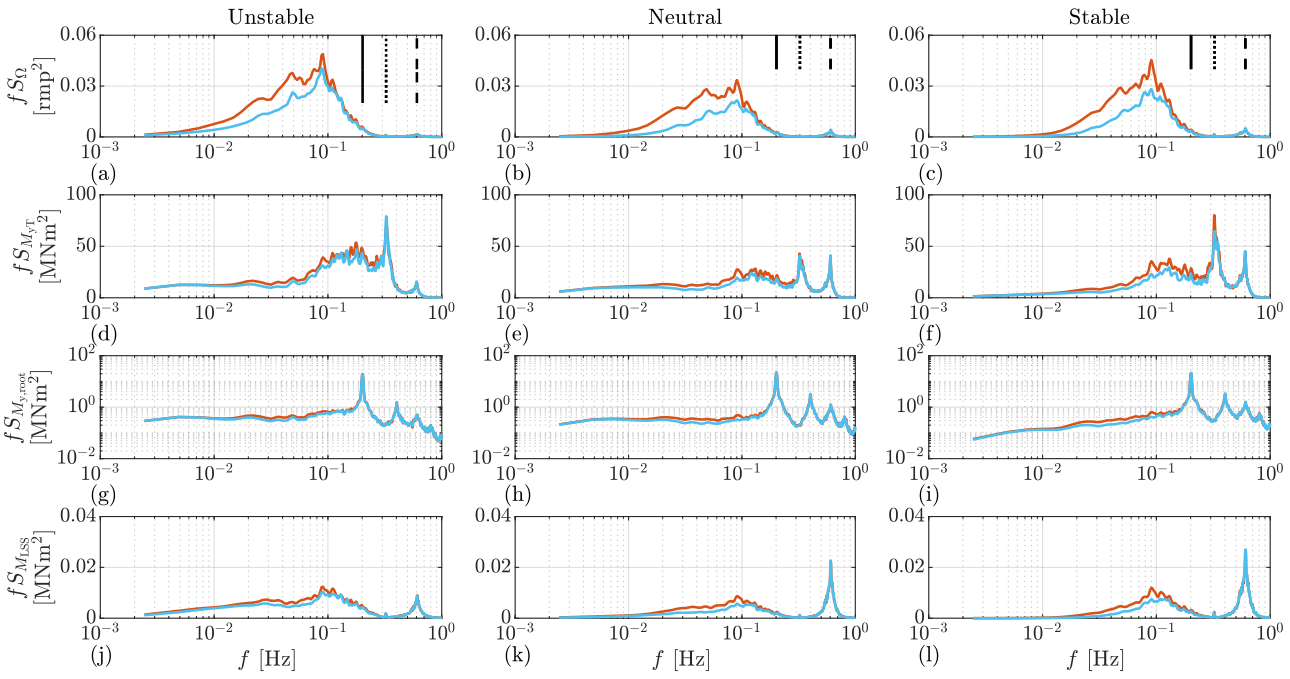

Figure 10. The auto-spectra estimated from OpenFAST output time series. The simulation results are obtained using Kaimal model. The mean wind speed is 16 ms^{-1}. Note that the y axis of the blade root bending moment is set to logarithmic for better readability.

5.2.3 Simulation statistic

To further assess the benefits of LAC, we calculate the DEL using the rain flow counting method with 2 $\times 10^6$ as a reference number of cycles and a lifetime of 20 years. Wöhler exponent of 4 is used for the tower fore-aft bending moment and the low-speed shaft torque. Wöhler exponent of 10 is used for the blade root out-of-plane bending moment. The averaged DEL is calculated from the results by different random seed numbers. The overall statics are compared and shown in Figure 11 and Figure 12. For rotor speed, pitch rate, and electrical power (P_{el}) signals, the standard deviation obtained by each simulation sample is calculated and then the mean value is calculated from all samples.

Mann model-based results

Figure 11 compares the DEL, STD, and EP (energy production) results by the Mann model. The difference between FB only and FFFB controls is plotted by the blue lines. Overall, the difference between FB-only control and FFFB control becomes observable when the mean wind speed is higher than 16 ms^{-1}.

There are overall obvious reductions of the tower fore-aft bending moment DEL in all the investigated atmospheric stability classes. The largest reduction is found to be 18.8% by a mean wind speed of 22 ms^{-1} and under an unstable atmosphere. In the unstable case, before 22 ms^{-1}, it can be seen that the reduction is more clear with higher wind speed. On the opposite, the reduction is larger at 16 ms^{-1} and 18 ms^{-1} under stable case. As for the neutral case, the benefits are the greatest close to

https://doi.org/10.5194/wes-2022-62
Preprint. Discussion started: 7 July 2022

18 ms^{-1}. However, with the mean wind speed of 14 ms^{-1} and in the unstable case, the FFFB is giving higher DEL than FB only control. This can be caused by a higher possibility to pass the transition range between the below-rated and the above-rated operations. The current feedforward pitch is activated only depending on the lidar estimated REWS, therefore a short interval of wind rise or drop can cause unnecessary pitch action in the transition range where the turbine thrust force is the highest.

As for the low-speed shaft torque, the DEL is reduced by around 4.5% under the unstable case and at a higher wind speed. While the reduction is about 2-2.5% and 1-1.5% under neutral and stable cases, respectively.

The DEL of the blade out-of-plane moment is reduced by introducing LAC. More benefits (about 2.5-5%) are found under unstable and neutral stability classes. In the stable stability, the reduction is better at 14 ms^{-1}, where the value is close to 4%, and it drops to 2% by higher wind speeds.

The standard deviation (STD) of rotor speed is found to be reduced significantly using FFFB control. The reductions are more than 20% and are up to 40%. Also, it can be seen the reductions are more significant under higher mean wind speeds, which is similar in all the three-atmosphere stability classes.

Introduction the FF pitch also generally helps to reduce pitch rate $\dot{\theta}$. The standard deviation of pitch rate are reduced clearly (about 5%) from 16 ms^{-1} to 22 ms^{-1} under the unstable stability. A similar reduction is found in the neutral class but the only difference is that the reduction stops at the mean wind of 20 ms^{-1}. In the stable atmosphere, the pitch rate only reduces with mean wind speeds smaller than 20 ms^{-1}. With a mean wind speed higher or equal to 20 ms^{-1}, the FFFB control has a higher standard deviation of pitch rate under stable stability.

As for the electrical power STD, it is reduced obviously by about 19% in unstable and neutral cases, and by around 15% in the stable case. It can be seen that the reduction becomes less when the mean wind speed goes higher in stable condition.

In all stability cases and mean wind speeds, the electricity productions are similar either using LAC or not.

Kaimal model-based results

The results using the Kaimal model are shown in Figure 12. Generally, under different stability classes and mean wind speeds, the statistics show a similar trend as the results obtained by the Mann model. However, the values show some differences.

In terms of tower fore-after bending moment, the reductions of DEL are about 15% with a mean wind speed from 18-22 ms^{-1} under the unstable condition and are about 10% in the mean wind speed 18-20 ms^{-1}. In the stable case, the reduction is close to 10% with the mean wind speed of 16 ms^{-1} and it drops wither higher mean wind speeds.

The results of low-speed shaft load DEL show some difference compared to that of the Mann model, mainly in the unstable case. Here, with the Kaimal model, the DEL reduction is higher at 16 ms^{-1} and it goes lower by higher mean wind speeds, which is opposite to the trend by the Mann model. On average, the shaft load is reduced by around 3%, 2%, and 1.6%, respectively, under the three investigated stability classes.

Generally, the reduction of the blade root load simulated using the Kaimal model is similar to that based on the Mann model. On average, the blade root DEL is reduced by around 4%, 3%, and 2.5%, respectively, under the three investigated stability classes.

https://doi.org/10.5194/wes-2022-62
Preprint. Discussion started: 7 July 2022

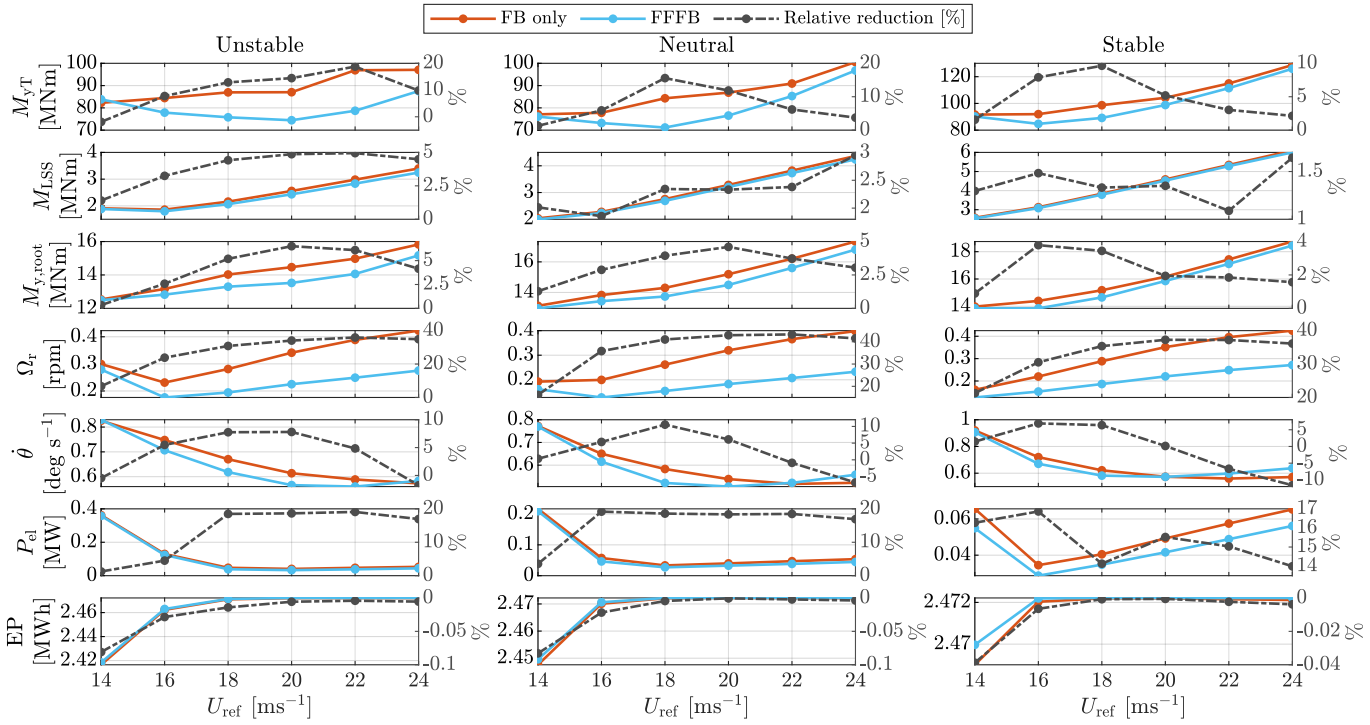

Figure 11. Comparison of DEL (M_{yT}, M_{LSS}, $M_{y,root}$), STD (Ω_r,$\dot{\theta}$,P_{el}), and EP, simulated using Mann model. Note that the value of the relative reduction are reflected by the right side y axis. Relative reduction: (FB only-FFFB)/(FB only).

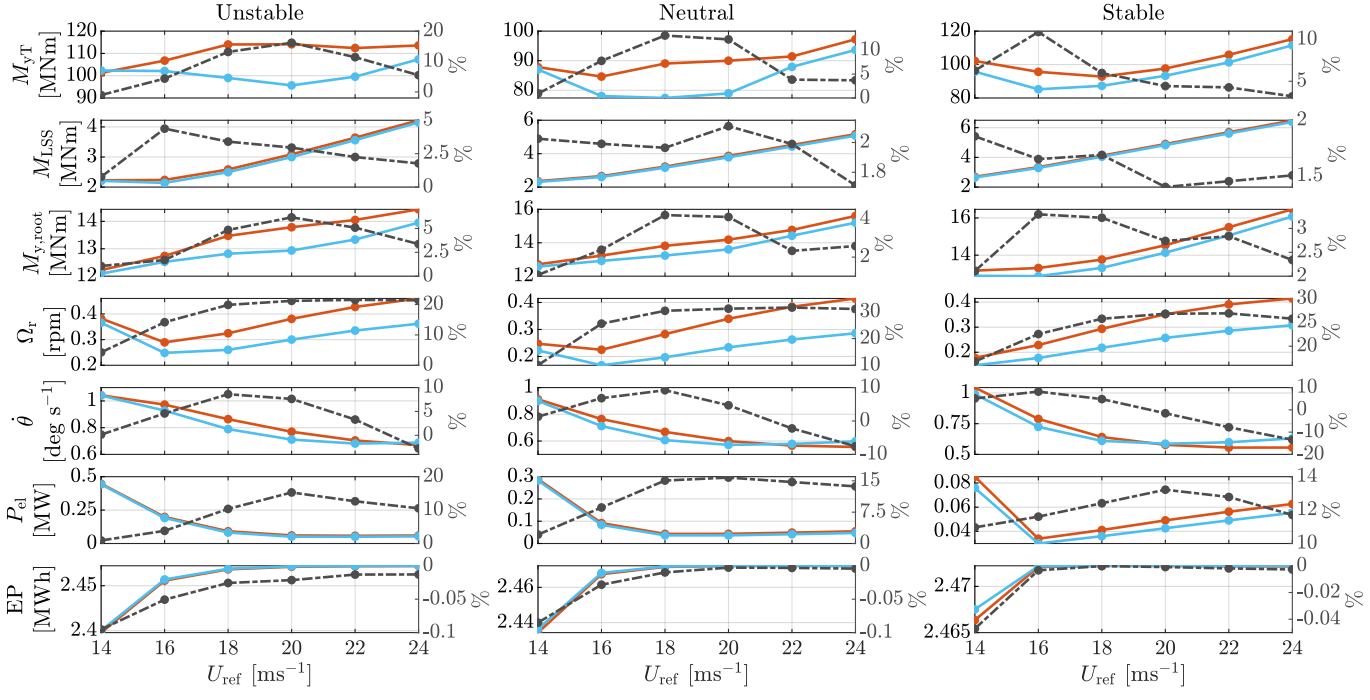

Figure 12. Comparison of DEL (M_{yT}, M_{LSS}, $M_{y,root}$), STD (Ω_r,$\dot{\theta}$,P_{el}), and EP, simulated using Kaimal model. Note that the value of the relative reduction are reflected by the right side y axis. Relative reduction: (FB only-FFFB)/(FB only).

https://doi.org/10.5194/wes-2022-62
Preprint. Discussion started: 7 July 2022

The STD of rotor speed is found to be reduced obviously using FFFB control. The reductions are more than 15% and are up to 30%. The trend is similar to the Mann model-based result but we can also see the reduction is a bit less than that shown by the Mann model.

The pitch actions show high similarity with that simulated using the Mann model. At 16 ms^{-1}, the reductions in pitch rate are about 8% under unstable and neutral stability classes and they become less in other mean wind speeds.

Since the variation in electrical power is highly linked with the rotor speed. The reductions in the STD of power lie around 10%, 15%, and 12%, respectively, under the three investigated stability classes. These values are smaller than observed using the Mann model.

Again, the electricity productions are similar either using LAC or not, in all stability cases, and mean wind speeds

In general, the benefits of LAC in load reduction by a four-beam lidar are clear. However, we also show that there are some uncertainties and differences when assessing LAC by different IEC turbulence models. Among the compared turbine load, LAC has the most significant load reduction effect in the tower base fore-aft bending moment. There are also considerable reductions in speed and power variations. The electrical power generation is not affected by introducing LAC. The load reductions also show differently under different turbulence parameters represented by different atmosphere stability.

6 Conclusions

This paper evaluates lidar-assisted wind turbine control under various turbulence characteristics using a four-beam liar and the NREL 5.0 MW reference turbine. The main contributions of this work include: 1) summarizing the turbulence spectra and the coherence under various atmosphere stability conditions, 2) analyzing the requirement of filter design for lidar-assisted wind turbine control under various turbulence characteristics, 3) developing a reference lidar-assisted control package, and 4) evaluating the benefits of lidar-assisted wind turbine control using the two turbulence through aeroelastic simulations.

Currently, two turbulence models (the Mann model and the Kaimal model) are provided by the IEC standard for turbine aeroelastic simulation. The recent research has made it possible to generate 4D stochastic turbulence fields in aeroelastic simulation for both the Mann model and Kaimal model, which allows for simulating lidar measurements more realistically and assessing the potential benefits by lidar-assisted control more reasonably. When evaluating the benefits of lidar-assisted control, previous research uses the Kaimal model with fixed turbulence spectral parameters provided by the IEC standard Schlipf (2015). Thus, the variations of turbulence characteristics by atmospheric stability have not been considered. In this study, we defined three turbulence cases whose characteristics are summarized from unstable, neutral, and stable atmospheric stability conditions. The turbulence spectrum and spatial coherence with separations in all directions are derived.

Based on the defined three turbulence cases, we analyzed the coherence between the lidar estimated rotor effective wind speed and the turbine-based rotor effective wind speed. The NREL 5.0 MW reference wind turbine and a four-beam pulsed lidar system are taken into consideration. It is found that some differences appear between the results of the Mann model and that of the Kaimal model. The coherence using the Mann model is generally higher in all atmospheric stability classes than the coherence using the Kaimal model. We further analyzed the transfer function, which is important for designing a filter,

https://doi.org/10.5194/wes-2022-62
Preprint. Discussion started: 7 July 2022

which removes uncorrelated content in the signal for lidar-assisted control. The analysis revealed that the difference for the transfer function between using different turbulence models or different stability classes is not very significant. This also means a simple linear filter design for lidar-assisted control is sufficient for various atmospheric stability conditions.

To further analyse the impact of atmospheric stability for lidar-assisted control, a reference lidar-assisted control package is developed and used in this work. The lidar-assisted control package includes several DLL modules written in FORTRAN: 1) a wrapper DLL that calls all sub-DLLs sequentially, 2) the lidar data processing DLL that estimates the rotor effective wind speed and records the leading time of the rotor effective wind speed, 3) a feed-forward pitch module that filters the rotor effective wind speed and activates the feed-forward rate at the correct time, 4) a modified reference FB controller (ROSCO) which can receive feed-forward command.

The benefits of lidar-assisted control are evaluated using both the Mann model and Kaimal model-based 4D turbulence. The simulations are performed for the mean wind speed level from 14 ms^{-1} to 24 ms^{-1}, using the NREL 5.0 MW reference wind turbine and a four-beam lidar system. For the results with the Mann model, using lidar-assisted control reduces the variations in rotor speed, pitch rate, and electrical power significantly. Among the three investigated stability classes and above the mean wind speed 16 ms^{-1}, the load reduction for the tower bending moment is found to be around 5.0% to 18.8%, and the load reduction for the blade root bending moment is found to be 1.5% to 5.5% and the load reduction for the low-speed shaft torque is around 1.2% to 5.0%. The greatest potential of lidar-assisted control in load reduction is found in the tower base loads and the benefits are found to vary by turbulence spectral proprieties and the mean wind speeds. For the results of the Kaimal model, using lidar-assisted control also reduces the variation in rotor speed, pitch rate, and electrical power clearly. The load reduction of the tower bending moment is found in all stability classes for wind speed above 16 ms^{-1} and it varies from 4.4% to 16.2%. The load reduction for the blade root bending moment is between 1.6% to 6.6% and for the the low-speed shaft torque between 1.4% to 4.4%. Overall, we found the lidar-assisted control benefits with the Kaimal model are slightly different from the results using the Mann model.

Overall, with this work, we show that the mean wind speed, the turbulence spectrum, coherence, and the used turbulence models all have certain impacts on the results of evaluating lidar-assisted control. In the future, we recommended assessing the benefits of lidar-assisted control depending on site-specific turbulence characteristics and statistics. Also, it is necessary to consider the uncertainties in turbulence models when performing load analysis using aero-elastic simulations. Further, some improvements can be made toward the lidar-assisted pitch forward control: The activation algorithm of the feedforward pitch in the transition range between the below-rated and the above-rated operations should be further improved.

Code availability. The OpenFASTv3.0 version with a lidar simulator integrated can be accessed via: https://github.com/fengguoFUAS/OpenFAST3.0_LidSim

The 4D Mann turbulence generator can be found by: https://github.com/fengguoFUAS/4D-Mann-Turbulence-Generator

The open-access tool *evoTurb* has been published on Github: https://github.com/SWE-UniStuttgart/evoTurb.

https://doi.org/10.5194/wes-2022-62
Preprint. Discussion started: 7 July 2022

eawe european academy of wind energy
Open Access WIND ENERGY SCIENCE DISCUSSIONS

Author contributions. FG conceived the concept, performed the simulations and prepared the manuscript. DS supported to verify the simulations, provided general guidance and reviewed the paper. PWC provided suggestions, revised and reviewed the paper.

Competing interests. The authors declare that they have no conflict of interest.

Acknowledgements. This research received financial supports from the European Union's Horizon 2020 research and innovation program under the Marie Skłodowska-Curie grant agreement No. 858358 (LIKE – Lidar Knowledge Europe).

https://doi.org/10.5194/wes-2022-62
Preprint. Discussion started: 7 July 2022

eawe european academy of wind energy
Open Access WIND ENERGY SCIENCE DISCUSSIONS

References

Abbas, N. J., Zalkind, D. S., Pao, L., and Wright, A.: A reference open-source controller for fixed and floating offshore wind turbines, Wind Energy Science, 7, 53–73, https://doi.org/10.5194/wes-7-53-2022, https://wes.copernicus.org/articles/7/53/2022/, 2022.

Bossanyi, E. A., Kumar, A., and Hugues-Salas, O.: Wind turbine control applications of turbine-mounted LIDAR, Journal of Physics: Conference Series, 555, 012 011, https://doi.org/10.1088/1742-6596/555/1/012011, 2014.

Chen, Y., Schlipf, D., and Cheng, P. W.: Parameterization of wind evolution using lidar, Wind Energy Science, 6, 61–91, https://doi.org/10.5194/wes-6-61-2021, 2021.

Chen, Y., Guo, F., Schlipf, D., and Cheng, P. W.: Four-dimensional wind field generation for the aeroelastic simulation of wind turbines with lidars, Wind Energy Science, 7, 539–558, https://doi.org/10.5194/wes-7-539-2022, https://wes.copernicus.org/articles/7/539/2022/, 2022.

Cheynet, E., Jakobsen, J. B., and Obhrai, C.: Spectral characteristics of surface-layer turbulence in the North Sea, Energy Procedia, 137, 414–427, 2017.

Davenport, A. G.: The spectrum of horizontal gustiness near the ground in high winds, Quarterly Journal of the Royal Meteorological Society, 87, 194–211, https://doi.org/10.1002/qj.49708737208, 1961.

Davoust, S. and von Terzi, D.: Analysis of wind coherence in the longitudinal direction using turbine mounted lidar, Journal of Physics: Conference Series, 753, 072 005, https://doi.org/10.1088/1742-6596/753/7/072005, https://doi.org/10.1088/1742-6596/753/7/072005, 2016.

Dimitrov, N., Natarajan, A., and Mann, J.: Effects of normal and extreme turbulence spectral parameters on wind turbine loads, Renewable Energy, 101, 1180–1193, https://doi.org/https://doi.org/10.1016/j.renene.2016.10.001, https://www.sciencedirect.com/science/article/pii/S0960148116308655, 2017.

DNV-GL: Bladed theory manual: version 4.8, Tech. rep., Garrad Hassan & Partners Ltd., Bristol, UK, 2016.

Dong, L., Lio, W. H., and Simley, E.: On Turbulence Models and LiDAR Measurements for Wind Turbine Control, Wind Energy Science Discussions, 2021, 1–16, https://doi.org/10.5194/wes-2021-51, https://wes.copernicus.org/preprints/wes-2021-51/, 2021.

Guo, F., Mann, J., Peña, A., Schlipf, D., and Cheng, P. W.: The space-time structure of turbulence for lidar-assisted wind turbine control, Renewable Energy, 195, 293–310, https://doi.org/https://doi.org/10.1016/j.renene.2022.05.133, https://www.sciencedirect.com/science/article/pii/S0960148122007844, 2022a.

Guo, F., Schlipf, D., Zhu, H., Platt, A., Cheng, P. W., and Thomas, F.: Updates on the OpenFAST Lidar Simulator, Journal of Physics: Conference Series, 2265, 042 030, https://doi.org/10.1088/1742-6596/2265/4/042030, https://doi.org/10.1088/1742-6596/2265/4/042030, 2022b.

Held, D. P. and Mann, J.: Lidar estimation of rotor-effective wind speed – an experimental comparison, Wind Energy Science, 4, 421–438, https://doi.org/10.5194/wes-4-421-2019, https://wes.copernicus.org/articles/4/421/2019/, 2019.

Hunt, J. C. and Carruthers, D. J.: Rapid distortion theory and the 'problems' of turbulence, Journal of Fluid Mechanics, 212, 497–532, 1990.

IEC 61400-1:2019: Wind energy generation systems – Part 1: Design requirements, Standard, International Electrotechnical Commission, Geneva, Switzerland, 2019.

Jonkman, B. J.: TurbSim user's guide: Version 1.50, Tech. rep., National Renewable Energy Lab.(NREL), Golden, CO (United States), 2009.

Jonkman, J., Butterfield, S., Musial, W., and Scott, G.: Definition of a 5-MW reference wind turbine for offshore system development, Tech. rep., National Renewable Energy Lab.(NREL), Golden, CO (United States), 2009.

Julier, S. J. and Uhlmann, J. K.: Unscented filtering and nonlinear estimation, Proceedings of the IEEE, 92, 401–422, 2004.

https://doi.org/10.5194/wes-2022-62
Preprint. Discussion started: 7 July 2022

Kaimal, J. C., Wyngaard, J. C., Izumi, Y., and Coté, O. R.: Spectral characteristics of surface-layer turbulence, Quarterly Journal of the Royal Meteorological Society, 98, 563–589, https://doi.org/10.1002/qj.49709841707, 1972.

Laks, J., Simley, E., and Pao, L.: A spectral model for evaluating the effect of wind evolution on wind turbine preview control, in: 2013 American Control Conference, pp. 3673–3679, IEEE, https://doi.org/10.1109/ACC.2013.6580400, 2013.

Mann, J.: The spatial structure of neutral atmospheric surface-layer turbulence, Journal of fluid mechanics, 273, 141–168, 1994.

Mann, J.: Wind field simulation, Probabilistic engineering mechanics, 13, 269–282, 1998.

Mann, J., Cariou, J.-P. C., Parmentier, R. M., Wagner, R., Lindelöw, P., Sjöholm, M., and Enevoldsen, K.: Comparison of 3D turbulence measurements using three staring wind lidars and a sonic anemometer, Meteorologische Zeitschrift, 18, 135–140, https://doi.org/10.1127/0941-2948/2009/0370, 2009.

Mirzaei, M. and Mann, J.: Lidar configurations for wind turbine control, Journal of Physics: Conference Series, 753, 032 019, https://doi.org/10.1088/1742-6596/753/3/032019, https://doi.org/10.1088/1742-6596/753/3/032019, 2016.

Nybø, A., Nielsen, F. G., Reuder, J., Churchfield, M. J., and Godvik, M.: Evaluation of different wind fields for the investigation of the dynamic response of offshore wind turbines, Wind Energy, 23, 1810–1830, 2020.

Peña, A., Mann, J., and Dimitrov, N.: Turbulence characterization from a forward-looking nacelle lidar, Wind Energy Science, 2, 133–152, https://doi.org/10.5194/wes-2-133-2017, 2017.

Peña, A.: Østerild: A natural laboratory for atmospheric turbulence, Journal of Renewable and Sustainable Energy, 11, 063 302, https://doi.org/10.1063/1.5121486, 2019.

Peña, A., Hasager, C. B., Lange, J., Anger, J., Badger, M., and Bingöl, F.: Remote Sensing for Wind Energy, Tech. Rep. DTU Wind Energy-E-Report-0029(EN), DTU Wind Energy, Roskilde, Denmark, 2013.

Schlipf, D.: Lidar-Assisted Control Concepts for Wind Turbines, Dissertation, University of Stuttgart, https://doi.org/10.18419/opus-8796, 2015.

Schlipf, D., Cheng, P. W., and Mann, J.: Model of the Correlation between Lidar Systems and Wind Turbines for Lidar-Assisted Control, Journal of Atmospheric and Oceanic Technology, 30, 2233–2240, https://doi.org/10.1175/JTECH-D-13-00077.1, 2013a.

Schlipf, D., Schlipf, D. J., and Kühn, M.: Nonlinear model predictive control of wind turbines using LIDAR, Wind Energy, 16, 1107–1129, https://doi.org/https://doi.org/10.1002/we.1533, https://onlinelibrary.wiley.com/doi/abs/10.1002/we.1533, 2013b.

Schlipf, D., Fürst, H., Raach, S., and Haizmann, F.: Systems Engineering for Lidar-Assisted Control: A Sequential Approach, Journal of Physics: Conference Series, 1102, 012 014, https://doi.org/10.1088/1742-6596/1102/1/012014, https://doi.org/10.1088/1742-6596/1102/1/012014, 2018a.

Schlipf, D., Hille, N., Raach, S., Scholbrock, A., and Simley, E.: IEA Wind Task 32: Best Practices for the Certification of Lidar-Assisted Control Applications, in: Journal of Physics: Conference Series, vol. 1102, p. 012010, IOP Publishing, 2018b.

Schlipf, D., Lemmer, F., and Raach, S.: Multi-variable feedforward control for floating wind turbines using lidar, in: The 30th International Ocean and Polar Engineering Conference, OnePetro, 2020.

Simley, E.: Wind Speed Preview Measurement and Estimation for Feedforward Control of Wind Turbines, ProQuest Dissertations & Theses, Ann Arbor, 2015.

Simley, E. and Pao, L.: Reducing LIDAR wind speed measurement error with optimal filtering, in: 2013 American Control Conference, pp. 621–627, https://doi.org/10.1109/ACC.2013.6579906, 2013.

Simley, E. and Pao, L.: A longitudinal spatial coherence model for wind evolution based on large-eddy simulation, in: 2015 American Control Conference (ACC), pp. 3708–3714, IEEE, https://doi.org/10.1109/ACC.2015.7171906, 2015.

https://doi.org/10.5194/wes-2022-62
Preprint. Discussion started: 7 July 2022

Simley, E., Fürst, H., Haizmann, F., and Schlipf, D.: Optimizing Lidars for wind turbine control applications—Results from the IEA wind task 32 Workshop, Remote Sensing, 10, 863, 2018a.

Simley, E., Fürst, H., Haizmann, F., and Schlipf, D.: Optimizing Lidars for Wind Turbine Control Applications—Results from the IEA Wind Task 32 Workshop, Remote Sensing, 10, https://doi.org/10.3390/rs10060863, https://www.mdpi.com/2072-4292/10/6/863, 2018b.

Taylor, G. I.: The spectrum of turbulence, Proceedings of the Royal Society of London. Series A-Mathematical and Physical Sciences, 164, 476–490, 1938.

von Kármán, T.: Progress in the statistical theory of turbulence, Proceedings of the National Academy of Sciences of the United States of America, 34, 530, 1948.

Welch, P.: The use of fast Fourier transform for the estimation of power spectra: a method based on time averaging over short, modified periodograms, IEEE Transactions on audio and electroacoustics, 15, 70–73, 1967.

Wiener, N. et al.: Extrapolation, interpolation, and smoothing of stationary time series: with engineering applications, vol. 8, MIT press Cambridge, MA, 1964.